



Synergistic activation of sulfate by TiO₂ nanotube arrays-based electrodes for berberine degradation: Insight into pH-dependant ORR-strengthened reactive radicals co-generation mechanism

Guoquan Zhang^{*}, Luying Zhao¹, Xiaoxin Hu¹, Xiaoyu Zhu, Fenglin Yang

Key Laboratory of Industrial Ecology and Environmental Engineering, Ministry of Education, School of Environmental Science and Technology, Dalian University of Technology, Linggong Road 2#, Dalian 116024, China

ARTICLE INFO

Keywords:

TiO₂ nanotube arrays
Synergistic sulfate activation
Reactive radicals co-generation
Sulfate radical
Berberine hydrochloride

ABSTRACT

An anodic oxidation-cathodic ORR coupling system originated from TiO₂ nanotube array (TNAs)-based electrodes was established. We first thoroughly investigated the effects of cell voltage, electrolyte type and pH on anodic reactive radicals co-generation and cathodic ORR pathway in the divided cells. Based on the results of anodic and cathodic half-reactions, the strengthening effect of the pH-dependant ORR process on the synergistic sulfate activation and reactive radicals co-generation mechanism were systematically elucidated in the undivided cells, by means of berberine degradation/mineralization degree and kinetics, electron spin resonance, radical quenching and energy consumption estimation. The real service lifetime of blue TNAs anode was evaluated, and the possible degradation pathways of berberine was also proposed. This pH-dependent ORR-strengthened synergistic sulfate activation system provide a multi-radical joint-attack mechanism for the pre-treatment or point-source-treatment of sulfate-containing refractory organics wastewater.

1. Introduction

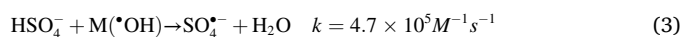
In recent decades, sulfate radical (SO₄^{•-})-based advanced oxidation processes (SR-AOPs) have gained increasing attention as an effective approach for the degradation and mineralization of toxic or recalcitrant organic pollutant in water and wastewater, due to their wide pH range, high redox potential (comparable to •OH) [1], long half-time (30–40 μs vs •OH < 1 μs) and high selectivity. SO₄^{•-} is commonly generated via the activation of peroxodisulfate (S₂O₈²⁻) and peroxymonosulfate (HSO₅⁻), by using heat (> 35 °C), alkaline (pH > 10.5), chemicals, transition metal, UV (< 400 nm), ultrasound or carbonaceous materials to split the peroxy bond ([O-O]²⁻) [2–6]. However, the potential secondary pollution, catalyst deactivation, high operation cost and energy input make these activation methods inapplicable for large-scale water treatment. Therefore, developing an efficient and simple technique for SO₄^{•-} generation and/or persulfate activation is a promising approach to promote the application of SR-AOPs in treating recalcitrant organic contaminants.

For a long time, sulfate electrolytes are considered inert in electrochemical advanced oxidation processes (EAOPs), while in recent years a

certain amount of literatures [3,7–18] reported that persulfate can be effectively produced with SO₄^{•-} as intermediates via the electrolysis of sulfate-containing solutions using non-active electrode, such as boron-doped diamond (BDD), PbO₂, SnO₂ or sub-stoichiometric TiO₂ via two pathways: (i) the direct discharge of sulfate ions (including HSO₄⁻ and SO₄²⁻) (Eq. (1) and Eq. (2)) at anode surface (M);



(ii) the indirect oxidation of sulfate ions via the physically adsorbed •OH (denoted as M(•OH)) (Eq. (3) and Eq. (4)).

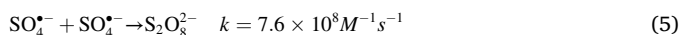


Eventually, SO₄^{•-} undergoes the further dimerization (Eq. (5)) yielding S₂O₈²⁻ [2,3,6].

^{*} Corresponding author.

E-mail address: guoquanz@126.com (G. Zhang).

¹ L. Zhao and X. Hu contributed equally to this work



Thus, the anode material with high oxygen evolution overpotential, especially BDD anode, plays a vital role in conversing $\text{SO}_4^{\bullet-}$ to SO_4^{2-} and $\text{S}_2\text{O}_8^{2-}$, under the action of weakly adsorbed BDD($\bullet\text{OH}$) [2,13]. Nevertheless, the complex fabrication and high cost of BDD stimulate the exploitation of affordable materials as an alternative.

Anodization growing the vertically oriented TiO_2 nanotube arrays (TNAs) with high aspect ratio from a Ti substrate has attracted considerable attention in the field of photo-electrochemical catalysis and EAOPs, because of the highly ordered TiO_2 nanostructure, large surface area and good corrosion resistant in both acidic and alkaline media [10]. However, the anodized TNAs usually show the low electrocatalytic activity in aqueous solution when used as anode, due to their semi-conductive nature. To overcome these disadvantages, great efforts have been dedicated to modifying the TNAs surface by the non-active anode materials, such as PbO_2 [7,19–22], $\text{SnO}_2\text{-Sb}_2\text{O}_3$ [23] and $\text{SnO}_2\text{-Sb}_2\text{O}_3/\text{PbO}_2$ composites [24–26]. Recent studies [3,8,10,27–32] have also demonstrated that the self-doping of TNAs through facile cathodic polarization can effectively improve the conductivity of TNAs, achieving an almost metallic behavior of TNAs film. This cost-effective and simplest modification method also can smartly manipulate the concentrations of Ti^{3+} sites (almost 1%) and oxygen vacancies via proton intercalation ($\text{Ti}^{4+} + \text{e}^- + \text{H}^+ \rightarrow \text{Ti}^{3+}\text{H}^+$) into TNAs [8,27]. After cathodic polarization the color of anatase TNAs changes from gray to blue, forming the so-called blue-TNAs (BTNAs), which possess the enhanced oxygen evolution overpotential and can be used as non-active anode with a comparable or even higher $\bullet\text{OH}$ production activity compared to BDD electrode [3,10,28]. On the other hand, M. A. Ghanem et al. [33] and J. Milikić et al. [34] demonstrated that the TNAs cathode can strongly promote interfacial electron transfer and effectively catalyze oxygen reduction reactions (ORR) into different products, depending on the different modification methods of TNAs.

Most focus were made on the anode half-reactions in SR-AOPs, for example, the combination of non-active anode and persulfate has been comprehensively investigated for the degradation of recalcitrant organic contaminants [35–40]. To our best knowledge, the cathodic ORR-stimulated synergistic activation of persulfate for reactive radicals co-generation has gained only limited attention [41–43], and nearly no study has focused on BTNAs anode//TNAs cathode pair for sulfate/persulfate activation. Although a few researches [42,43] have conducted on persulfate activation by means of the combined anodic oxidation and the cathodic in-situ electrogenerated H_2O_2 , but the mechanisms behind this activation process is still not clear [5]. Therefore, it is of great significance to investigate reactive radicals co-generation in sulfate-containing solutions via anodic oxidation/cathodic ORR by using TNAs-based electrodes.

As a broad-spectrum antibiotic medicine, berberine hydrochloride has been widely used against a wide variety of microorganisms including Gram-positive and Gram-negative bacteria, and fungi et al. [44], however, which can not be fully absorbed by animals, and a considerable part was discharged into environment in the form of proto-molecules or metabolites, which not only destroy the ecological balance, but also can produce resistance genes induced by the pathogenic microorganisms.

Herein, an anodic oxidation-cathodic ORR coupling system was constructed using the TNAs-based electrodes (BTNAs or $\beta\text{-PbO}_2/\text{TNAs}$ as anode and TNAs-N_2 as cathode) to destroy berberine ($\text{C}_{20}\text{H}_{18}\text{NO}_4$). We thoroughly investigated the effects of the applied cell voltage, electrolyte type and pH on anodic active radicals co-generation and cathodic ORR pathway in the divided cells. Based on the results of anodic and cathodic half-reactions, the pH-dependent ORR-strengthened synergistic sulfate activation system was established and investigated in the undivided cells, and then the multi-radical co-generation and joint-attack mechanism were elucidated in-detail according to berberine degradation/mineralization degree, electron spin resonance (ESR),

radical quenching and energy cost estimation. Additionally, the service lifetime and stability of BTNAs and $\beta\text{-PbO}_2/\text{TNAs}$ anodes were evaluated, and the degradation intermediates were analyzed by liquid chromatography-mass spectrometry (LC-MS) measurements, from which the possible degradation pathways of berberine was also proposed.

2. Experimental

2.1. Preparation of vertically aligned TNAs-based electrodes

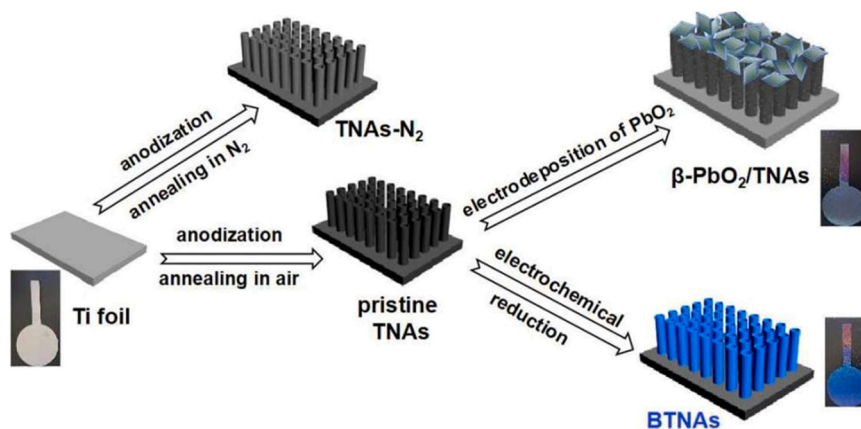
Ti foil with a nominal reaction area of 10.5 cm^2 (1.83 cm of radius, purity 99.6%, Sigma-Aldrich) were first degreased by ultrasonication in acetone and isopropanol mixture for 10 min, followed by mechanically polished by silicon carbide abrasive papers with sequentially finer roughness (600, 800, 1000 and 1500 mesh). After washing with deionized water and drying at room temperature, the chemical etching was performed in HF and HNO_3 mixture ($V_{\text{HF}}:V_{\text{HNO}_3}:V_{\text{H}_2\text{O}} = 1:4:5$) for 60 s and then rinsed by deionized water to obtain a fresh surface. TNAs that grown on the cleaned Ti surface was obtained via a two-step electrochemical anodization method [10]. The first anodization was performed at a constant voltage of 50 V (DP605C, MESTEK®) for 1 h in an ethylene glycol solution containing NH_4F (0.5 wt%) and H_2O (2.5 wt%) in an undivided cell with Ti plate as the anode placed at a distance of 2.5 cm from a Pt foil as the cathode. After dissolving the formed film in HNO_3 and HF mixture ($V_{\text{HF}}:V_{\text{HNO}_3} = 1:1$) and washing by the deionized water, the second anodization was performed in ethylene glycol solution containing NH_4F (0.25 wt%), HF (0.05 wt%) and H_2O (2 wt%) at 50 V for 6 h. This brown colored amorphous TNAs were cleaned in ethanol and annealed at 500°C for 2 h with a heating rate of 2°C min^{-1} under atmospheric condition, converting into the gray colored crystalline anatase TNAs [10,19]. The BTNAs were prepared by cathodic polarization using a galvanostatic method at 10 mA/cm^2 current density for 20 min in 10% formic acid solution. Due to the semiconductive nature of the anatase TNAs, the Ti/TNAs was electrochemically reduced for 60 s in 1 M $(\text{NH}_4)_2\text{SO}_4$ at a potential of -1.5 V vs Ag/AgCl to increase its conductivity for subsequent galvanostatic anodic electro-deposition of $\beta\text{-PbO}_2$ ($\beta\text{-PbO}_2/\text{TNAs}$), which was performed in 0.1 M HNO_3 solution containing 0.5 M $\text{Pb}(\text{NO}_3)_2$ and 0.05 M KF at 15 mA/cm^2 for 1.5 h at 65°C with continuous stirring [24]. The cathode used in this work was obtained by annealing the amorphous TNAs at 500°C for 2 h in N_2 atmosphere, labeled as TNAs-N_2 . The synthesis routes of TNAs-based samples were illustrated in Scheme 1.

2.2. Physicochemical characterization

The morphology of the prepared samples were evaluated by field-emission scanning electron microscopy (FESEM, Quanta FEG 250, FEI) equipped with an energy-dispersive X-ray spectroscopy detector. Crystalline nature were analyzed using a powder X-ray diffraction (XRD, Rigaku D/max-2400, Japan) with a nickel-filtered $\text{Cu-K}\alpha$ radiation source ($\lambda = 1.5406 \text{ \AA}$) as a monochromatic detector at 40 kV and 100 mA over a 2θ range of 10° to 80° . X-ray photoelectron spectroscopy (XPS, VG ESCALAB 250, Thermo Fisher) was used to characterize the surface composition of samples using a non-monochromatized $\text{Al-K}\alpha$ X-ray source ($h\nu = 1486.6 \text{ eV}$). All binding energies were corrected using C 1 s peak (284.5 eV). Raman spectroscopy was recorded at ambient temperature on a spectrometer (Renishaw InVia, model 2000) in the backscattering geometry with a 200 mW Ar^+ laser at 514.5 nm wavelength as an excitation source.

2.3. Electrochemical characterization

The detailed information for the electrochemical behaviors of pristine TNAs, $\beta\text{-PbO}_2/\text{TNAs}$, BTNAs and TNAs-N_2 electrodes, including CV, LSV, EIS, RDE and accelerated life tests was described in the Supporting



Scheme 1. Schematic illustration for the fabrication process of different TNAs-based materials.

Information S1.

2.4. Electrochemical degradation experiments

The detailed information of the electrocatalytic degradation procedures of berberine was described in the [Supporting Information S2](#).

2.5. Analysis methods

The detailed information of the analysis methods is provided in the [Supporting Information S3](#).

3. Results and discussion

3.1. Characterizations of the TNAs-based electrodes

The top and cross-sectional images of the pristine TNAs were first investigated by FESEM. As shown in [Fig. 1a](#) and [b](#), the TiO₂ nanotubes grow vertically on the Ti foil substrate, forming the highly ordered and vertically oriented nanotube arrays with the tube length of ca. 4.64 μm. [Fig. 1c-g](#) present the top and lateral morphologies of BTNAs and TNAs-N₂ samples, which exhibit the well-aligned high-density nanotube structures with average tube outer diameters of about 100.8 nm, tube length of 5.12 μm and tube wall thicknesses of 10.2 nm, indicating no noticeable morphology damage during the electrochemical reduction and calcination in N₂. After the electrochemical reduction of anatase TNAs at −1.5 V vs Ag/AgCl for 60 s, PbO₂ grains were successfully

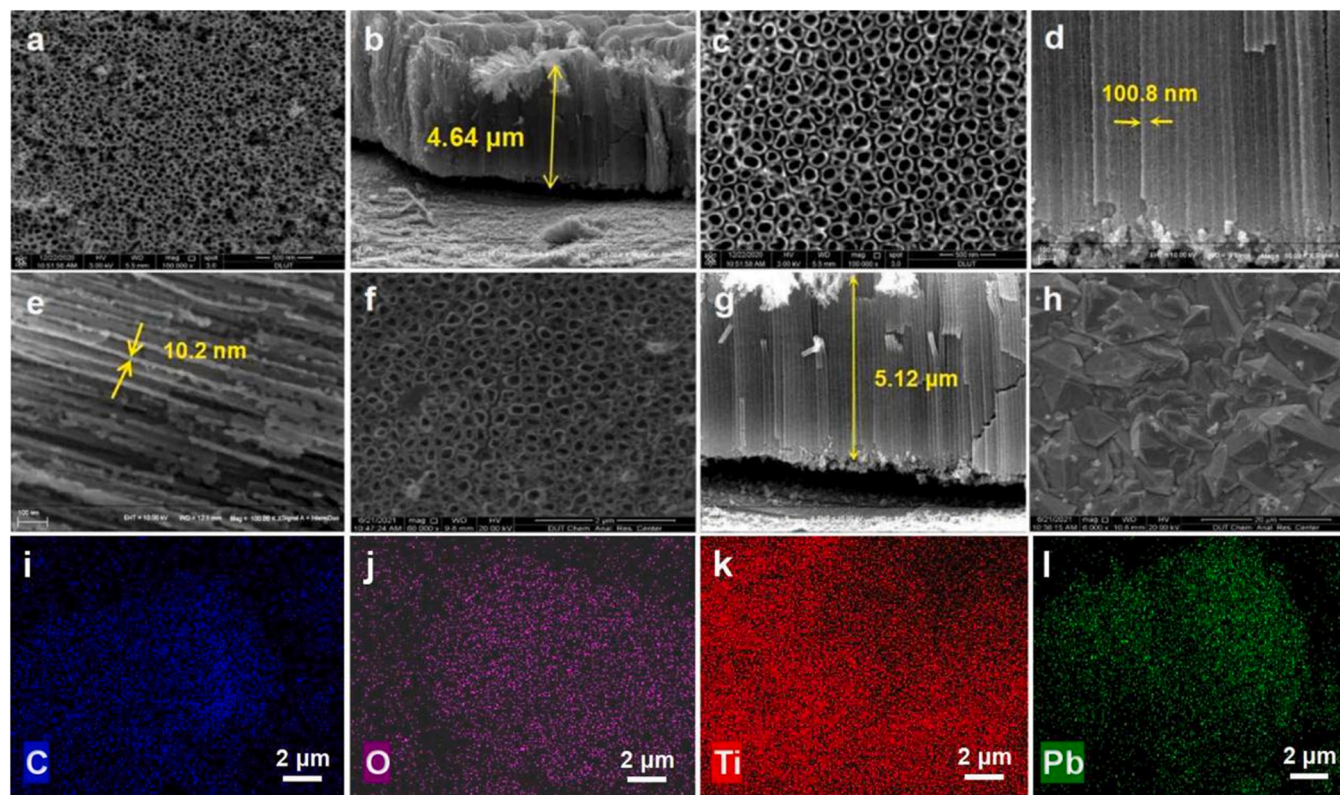


Fig. 1. SEM images of the top and lateral views: (a), (b) pristine TNAs, (c)-(e) BTNAs, (f) and (g) TNAs-N₂, (h) SEM image of top view of β-PbO₂/TNAs, (i)-(l) C, O, Ti and Pb element mapping images of BTNAs and β-PbO₂/TNAs samples, respectively.

deposited onto anatase TNAs arrays (Fig. 1e and f), forming the typical pyramidal shape with an average dimension of 5 μm . The compact coverage and uneven surface are believed beneficial to gain a better electro-oxidation activity [7,20]. Moreover, the SEM-EDX mapping images shown in Fig. 1i-l displayed the uniform distribution of C, O, Ti, and Pt elements within BTNAs and $\beta\text{-PbO}_2/\text{TNAs}$ samples.

The XRD spectrum of the pristine TNAs (Fig. 2a) presents seven predominant peaks at $2\theta = 25.3^\circ, 37.9^\circ, 48.2^\circ, 54.0^\circ, 55.2^\circ, 62.9^\circ$ and 70.6° , corresponding to (101), (103), (200), (105), (211), (204) and (220) planes of the tetragonal anatase TiO_2 phase (JCPDS 21-1272, I_{41}/amd , $a=b=0.379\text{ nm}$, $c=0.951\text{ nm}$), respectively [10,30]. Both BTNAs and TNAs- N_2 patterns maintain the same anatase TiO_2 crystal phase, while the reflection intensities of BTNAs are weaker than that of the pristine TNAs, owing to the formation of Ti^{3+} in the TiO_2 lattices after cathodic polarization [8,27]. No TiO_2 diffraction peaks was detected after PbO_2 deposition, and the corresponding XRD pattern exhibits the tetragonal plattnerite crystalline phase with the characteristic diffraction peaks at $2\theta = 25.2^\circ, 31.8^\circ, 36.0^\circ, 49.1^\circ, 52.0^\circ, 58.9^\circ, 62.3^\circ$ and 74.3° , which are indexed to the (110), (101), (200), (211), (220), (310), (301) and (321) planes of $\beta\text{-PbO}_2$ (JCPDS 41-1492) [19,20]. In addition to $\beta\text{-PbO}_2$ characteristic reflections, two weak diffraction peaks at $2\theta = 66.8^\circ$ and 78.2° indicate the presence of orthorhombic $\alpha\text{-PbO}_2$. On the other hand, the TiO_2 (004) diffraction peak of $\beta\text{-PbO}_2/\text{TNAs}$ disappears as compared to those of other TNAs samples, implying the good coverage of $\beta\text{-PbO}_2$ coating.

Raman spectra shown in Fig. 2b reveal that the pristine TNAs possesses six Raman active modes ($3\text{E}_g + 2\text{B}_{1g} + \text{A}_{1g}$), which can be assigned for 144.3 cm^{-1} (E_g), 197.4 cm^{-1} (E_g), 395.6 cm^{-1} (B_{1g}), 514.8 cm^{-1} ($\text{A}_{1g} + \text{B}_{1g}$) and 639.6 cm^{-1} (E_g), corresponding to the typical fingerprint of tetragonal anatase phase [30,45]. The same modes are also observed in the spectra of BTNAs and TNAs- N_2 samples, meaning that both the samples are composed of anatase phase. Notably, an obvious blue-shift and band-broadening of the main active mode peaks are also found in BTNAs and TNAs- N_2 samples compared to the pristine TNAs, which should be originated from the structural disorder and defects like Ti^{3+} self-doping and oxygen vacancies production [8,27,46]. For the $\beta\text{-PbO}_2/\text{TNAs}$ sample, three characteristic Raman peaks corresponding to E_g , A_{1g} , and B_{2g} modes are obtained at ca. 424.4 , 516.2 and 653.3 cm^{-1} , respectively, implying the existence of PbO_2 [47].

XPS measurements were carried out to further analyze the chemical compositions and valence states of the prepared samples. The XPS survey spectra (Fig. S1) confirms the presence of Ti, O and C elements in pristine TNAs, BTNAs and TNAs- N_2 samples, while the obvious Pb

element signals accompanying the weak Ti 2p signals were detected in the survey spectrum of $\beta\text{-PbO}_2/\text{TNAs}$, because of the compact PbO_2 coating over NTAs surface. As demonstrated in Fig. 3, the Ti 2p core-level XPS spectrum of pristine TNAs exhibits two peaks at 458.6 eV (Ti 2p $_{3/2}$) and 464.2 eV (Ti 2p $_{1/2}$), which can be assigned to Ti^{4+} [27,30]. Except for the above-mentioned similar characteristic Ti 2p $_{3/2}$ and Ti 2p $_{1/2}$ doublet structure, the corresponding shoulder peaks located at 457.9 and 463.6 eV were also observed in BTNAs and TNAs- N_2 samples, which are resulted from the self-doping of Ti^{3+} [10,29,30]. A qualitative comparison of Ti^{3+} concentration indicates that more Ti^{3+} sites (62.2% and 25.4% for BTNAs and TNAs- N_2 , respectively) were generated during the cathodic polarization, which is beneficial to improve the electro-activity of BTNAs. These results consist with previous reports [27,45] that the cathodic polarization produces no significant change in the surface properties of blue NTAs. The high-resolution Pb 4f XPS spectrum of $\beta\text{-PbO}_2/\text{TNAs}$ can be deconvoluted into two peaks centered at 138.0 eV (4f $7/2$) and 142.9 eV (4f $5/2$) with the binding energy difference of ca. 4.9 eV , which was identified as the particular spectral values of $\beta\text{-PbO}_2$ (Pb^{4+}) [22,23].

3.2. Electrochemical performance of the TNAs-based electrodes

Fig. 4a and b present the CV curves of $\beta\text{-PbO}_2/\text{TNAs}$ and BTNAs in N_2 -saturated $0.1\text{ M Na}_2\text{SO}_4$ electrolyte. As seen, the BTNAs exhibits the quasi-rectangular curves with typical semi-metallic capacitance characteristic [8,29] in the potential range of $-1.0 \sim 2.5\text{ V}$. The CV curve of $\beta\text{-PbO}_2/\text{TNAs}$ reveals a typical behavior of PbO_2 electrode [19], whereas that of the pristine TNAs shown in Fig. S2 displays a triangular shape as a characteristic of n-type semiconductor [10,28]. These results indicate that the generated Ti^{3+} site (oxygen vacancies) by the cathodic polarization leads to the BTNAs higher conductivity [27,30], as verified from the results of Fig. 3. The direct electron transfer reaction between berberine molecules and anodes were not observed in the potential region below oxygen evolution potential, implying that no berberine degradation by direct anodic oxidation occurs on all three electrodes. It is also necessary noting that no current increase corresponding to the direct discharge of HSO_4^- was found on the CVs, which suggests that SO_4^{2-} generation by the direct discharge of sulfate ions is negligible on the two investigated anodes.

EIS tests were also conducted to further evaluate the interfacial characteristics of the TNAs-based materials. Nyquist curves and an equivalent circuit model fitted by Zsimpwin software. As seen from Fig. 4c, each sample shows two semicircle arc from high to medium

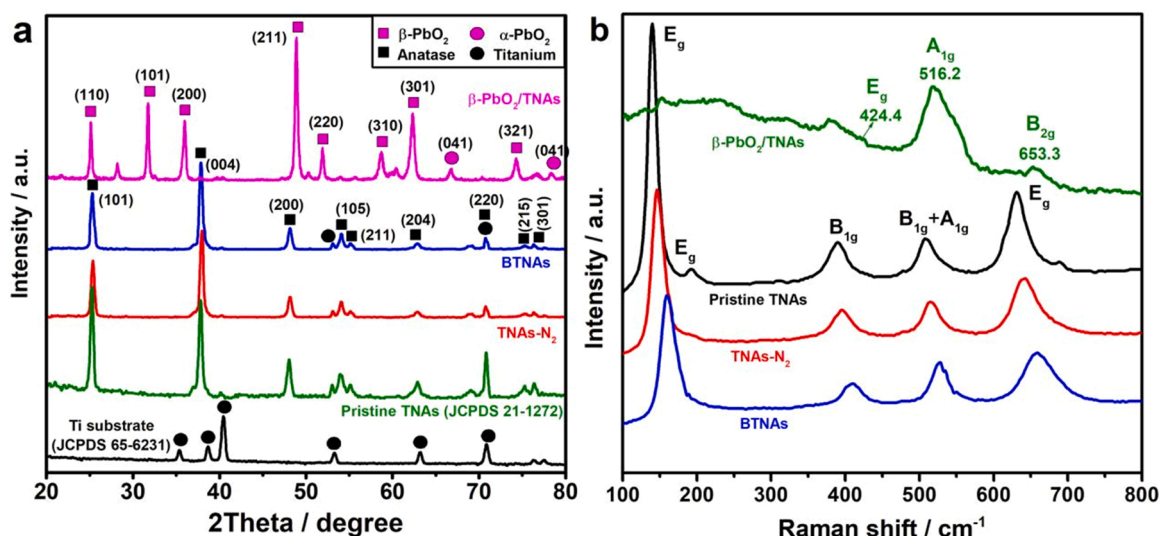


Fig. 2. (a) XRD patterns of titanium substrate (JCPDS 65-6231) and the prepared TNAs-based materials, (b) Raman spectra of different TNAs-based materials.

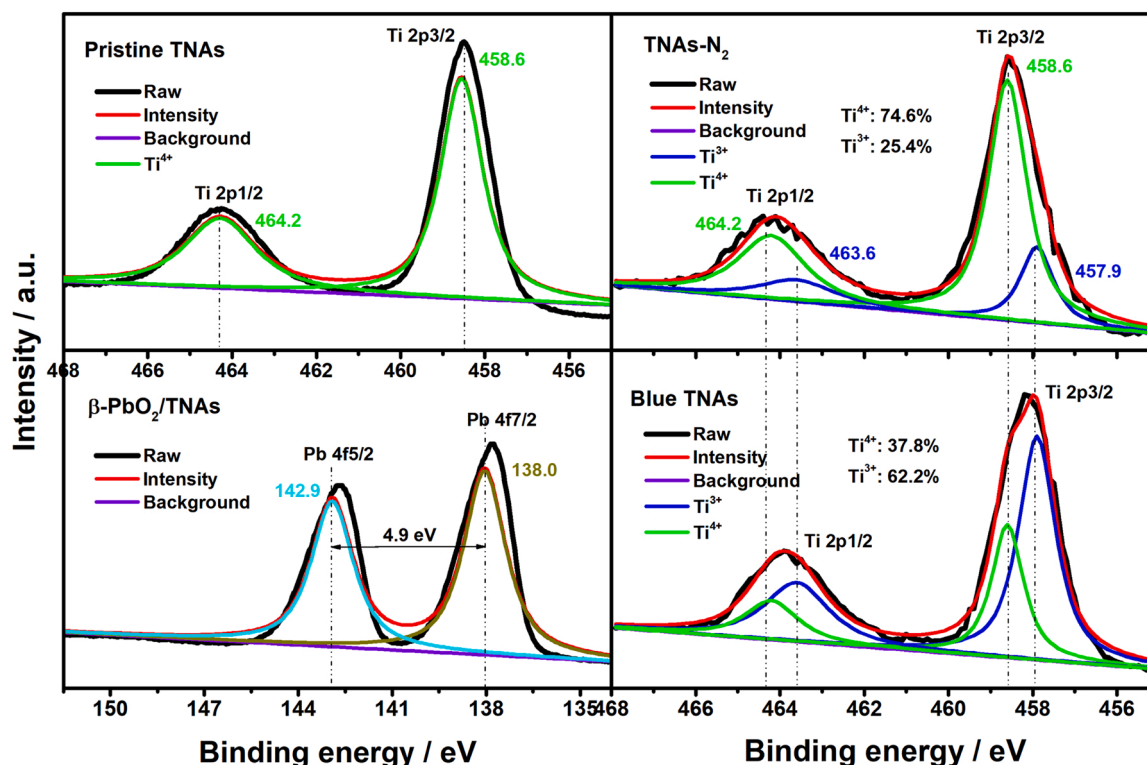


Fig. 3. The high-resolution core-level XPS spectra of Ti 2p and Pb 4f of various TNAs-based materials.

frequency, where the first one is attributed to the contact resistance between the active material and the current collector, and the second is caused by the charge transfer at the solid/electrolyte interface. Fitting results listed in Table S1 show that other three samples exhibit much smaller diameter of the semicircle arc when compared with that of pristine TNAs, illustrating the significantly depressed charge-transfer resistance and the enhanced electron-transfer efficiency. The BTNAs sample has the smallest charge-transport resistances through the nanotubes (R_{ct1} , 23.7 Ω) and at the electrode/electrolyte interface (R_{ct2} , 56.8 Ω), which indicates again the improved electrical conductivity owing to the electrochemical reduction incurred Ti^{3+} states/oxygen vacancies defects.

The OER performances of the pristine TNAs, β - PbO_2 /TNAs and BTNAs electrodes were assessed by LSV tests in 0.1 M H_2SO_4 electrolyte at a scan rate of 20 mV/s. According to Fig. 4d, there is no anodic response up to 3.0 V for the pristine TNAs due to its n-type semiconductor feature. After the cathodic polarization, the BTNAs displays a metallic-like property [28–30] with a higher OER potential (2.63 V vs Ag/AgCl) than that of β - PbO_2 /TNAs (2.07 V), which can efficiently facilitate reactive radicals generation and reduce energy consumption during the electro-oxidation treatment [7,8].

Hydrodynamic RDE polarization tests were performed on the TNAs- N_2 cathode in various pH O_2 -saturated Na_2SO_4 solutions to investigate ORR pathway and mechanism. As seen from Fig. 5, the current density increases with the increasing rotation rate due to the thin diffusion layer at high rotating rate. The diffusion-controlled limiting currents at pH 9.0 are higher than those at pH 3.0 and 12.0, which hints the better electrocatalytic activity for ORR. Besides, the Koutecky-Levich plots recorded at pH 9.0 and 12.0 in potential range from -1.1 to -0.6 V display good linear relationship, and the transferred electron number, n , are closed to 2 (Fig. 5c), implying that the TNAs- N_2 cathode proceeds mainly by a $2e^-$ ORR mechanism to form H_2O_2 . More obvious prewaves were clearly observed between -0.3 and -0.5 V at pH 12.0, which corresponds to the charge transfer to oxygen mediated by the surface-confined redox active species on TNAs- N_2 surface (Eq. (6)) [48,49]. As

the bulk electrolysis further progressed to more negative than -0.6 V, the ORR was primarily mediated by the surface Ti^{3+}/Ti^{4+} redox sites (Eq. (7)). Subsequently, the formed superoxide radical anions, $O_2^{\cdot-}$, would undergo following conversion process [6,34,48]: (i) reacting with H^+ to produce HO_2^{\cdot} in acidic pH (Eq. (8)), (ii) further one-electron reduction to form H_2O_2 or HO_2^- (Eqs. (9) and (10)), and (iii) disproportionation to HO_2^- in alkaline media (Eq. (11)).



Considering the different OER activity of β - PbO_2 /TNAs and BTNAs anodes as well as the potential-dependent $2e^-$ -ORR selectivity of TNAs- N_2 cathode, the potential distribution between anode (E_a) and cathode (E_c) of β - PbO_2 /TNAs//TNAs- N_2 and BTNAs//TNAs- N_2 pairs was measured in an undivided cell containing various pH O_2 -saturated 0.1 M Na_2SO_4 solution by the stepwise increased constant cell voltage (E_{cell}). As illustrated in Fig. 6, the $|E_a|$ value is always larger than that of $|E_c|$ at a given E_{cell} , which suggests that the potential distribution is not equal between E_a and E_c (i.e., $E_{cell} = |E_a| + |E_c|$, but $|E_a| \neq |E_c|$) even if both electrodes possess the same geometric size. In comparison to E_a , the applied E_{cell} ranging from 2.0 to 4.5 V brought greater effect on E_c for both two electrode pairs in all pH cases. Moreover, with regard to each electrode pair operating at given E_{cell} , electrolyte pH shows a significant impact influence on E_c . Above results demonstrated that imposing different E_{cell} leads to various effects on both E_a and E_c under the different pH conditions, which dominates O_2 -filling in oxygen vacancies

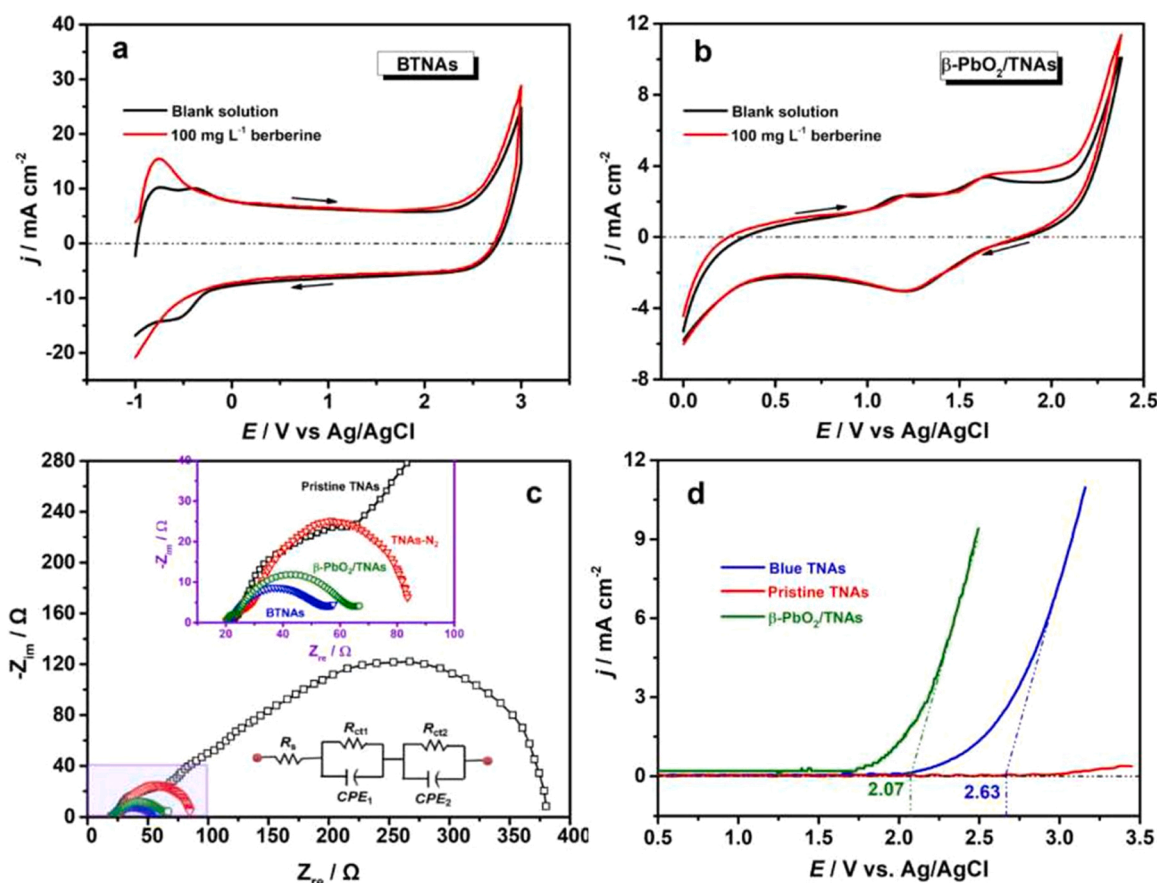


Fig. 4. CV curves of (a) BTNAs and (b) β -PbO₂/TNAs recorded in 0.1 M Na₂SO₄ electrolyte in the absence and presence of 100 mg/L berberine with a scan rate of 20 mV/s, (c) EIS Nyquist plots of different TNAs-based electrodes in 0.1 M Na₂SO₄ electrolyte at room temperature collected at the open-circuit potential in a frequency range of 100 kHz–10 mHz, and the insets show the magnified views in high-frequency region and the equivalent circuit model, (d) LSV curves of different TNAs-based anodes recorded in 0.1 M H₂SO₄ at a scan rate of 20 mV/s.

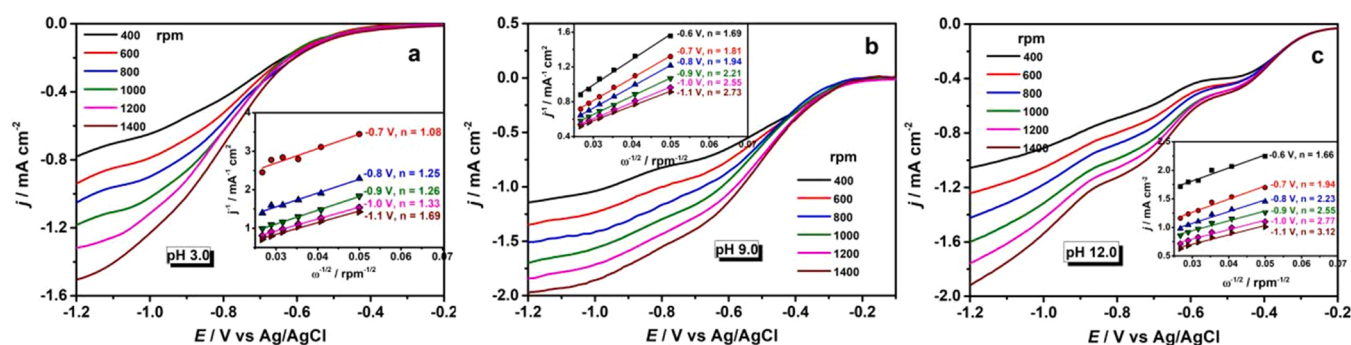


Fig. 5. RDE polarization curves of TNAs-N₂ cathode in O₂-saturated 0.1 M Na₂SO₄ electrolyte at different pH values: (a) 3.0, (b) 9.0 and (c) 12.0. The insets display the corresponding Koutecky-Levich plots and the electron transfer numbers, n , at different potentials.

of β -PbO₂/TNAs and BTNAs anodes [50] as well as the ORR pathways or products of TNAs-N₂ cathode.

3.3. Berberine degradation and reactive radicals generation in a divided cell

3.3.1. Reactive radicals generation and identification

The electro-generation of reactive radicals using β -PbO₂/TNAs and BTNAs anodes was evaluated in a divided cell containing 0.1 M Na₂SO₄ or NaNO₃ solution by potentiostatic electrolysis. Generally, two indirect methods, i.e. electron spin resonance (ESR) spectroscopy and probe compounds, are primarily employed for $\cdot\text{OH}$ detection. Although

different $\cdot\text{OH}$ probe molecules were employed in various AOPs, however, according to B. P. Chaplin et al. [51], most of the probes are susceptible to or can react by direct electron transfer reaction and Forrester-Hepburn mechanisms, resulting in the false positive detection of $\cdot\text{OH}$ and therefore are not appropriate probes. They also pointed out that an appropriate $\cdot\text{OH}$ probe should be electrochemical inertness and react with $\cdot\text{OH}$ at diffusion-limited rate yielding a stable product that can be detected by conventional chromatographic techniques. In terms of high second-order rate constant ($1.3 \times 10^{10} \text{ M}^{-1} \text{ s}^{-1}$), high selectivity and excellent electrochemical inertness, N, N-dimethyl-p-nitrosoaniline (RNO) was used as the probe compound to detect $\cdot\text{OH}$ via spectrophotometrical monitoring [7,20]. As seen from

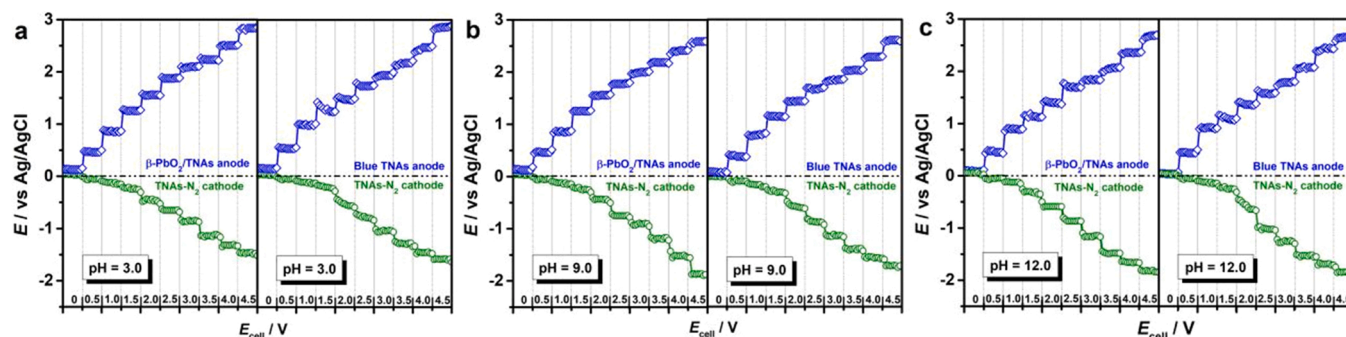


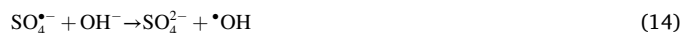
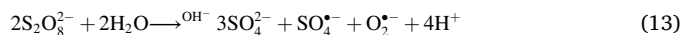
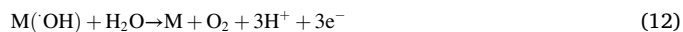
Fig. 6. Change of anode and cathode potentials of β -PbO₂/TNAs//TNAs-N₂ and BTNAs//TNAs-N₂ electrode pairs as a function of applied cell voltage (E_{cell}) in an undivided cell containing O₂-saturated 0.1 M Na₂SO₄ solution at different pH values: (a) 3.0, (b) 9.0, and (c) 12.0.

the adsorption spectra in Fig. S3, a quicker absorbance decline at the characteristic wavelength of 440 nm is found for BTNAs in 0.1 M Na₂SO₄ solution during potentiostatic electrolysis at $E_{\text{cell}} = 4.0$ V, which is more evident from the RNO bleaching kinetics analysis (Fig. 7a), implying the more efficient production of reactive radicals on BTNAs than on β -PbO₂/TNAs. Additionally, no intermediates absorption bands were observed at 245 and 323 nm, indicating both β -PbO₂/TNAs and BTNAs are the non-active anodes that able to produce the physically adsorbed $\cdot\text{OH}$ [19–21,27–30]. Nitrate is generally considered as an inert electrolyte at non-active anodes while sulfate can be converted into $\text{SO}_4^{\cdot-}$ [13]. Therefore, the significantly improved RNO decolorization in Na₂SO₄ electrolyte illustrates the simultaneous generation of higher concentrations of $\cdot\text{OH}$ and additional $\text{SO}_4^{\cdot-}$ (Eq. (1)–(3)) by using BTNAs anode.

The ESR spin-trapping technique using 5,5-dimethyl-1-pyrrolidine N oxide (DMPO) was applied to probe various radical species generated by β -PbO₂/TNAs and BTNAs anodes (Fig. 7b). Four equidistant and high-intensity DMPO- $\cdot\text{OH}$ adduct characteristic signals with intensity ratio of about 1:2:2:1 were observed in NaNO₃ electrolyte, while six low-intensity peaks with intensity ratio of approximately 1:1:1:1:1:1 that assigned to DMPO- $\text{SO}_4^{\cdot-}$ adduct [9,14,16] were detected along with DMPO- $\cdot\text{OH}$ signals in Na₂SO₄ electrolyte. Above ESR results further verify the simultaneous formation of both $\cdot\text{OH}$ and $\text{SO}_4^{\cdot-}$ during the electrochemical activation of sulfate by β -PbO₂/TNAs and BTNAs anodes at the applied voltage. The stronger characteristic signals demonstrate that more $\cdot\text{OH}$ and $\text{SO}_4^{\cdot-}$ were generated by BTNAs anode than by β -PbO₂/TNAs anode.

Previous studies [13–17] have validated that sulfate can be oxidized into $\text{S}_2\text{O}_8^{2-}$ at a non-active anode via the solution phase dimerization of $\text{SO}_4^{\cdot-}$ (Eq. (5)), thus it is necessary to evaluate the amount of $\text{S}_2\text{O}_8^{2-}$ formed during water oxidation in bulk Na₂SO₄ electrolytes using β -PbO₂/TNAs and BTNAs anodes, although $\text{S}_2\text{O}_8^{2-}$ is not always qualified for organics degradation owing to lower redox potential ($E^0(\text{S}_2\text{O}_8^{2-}/\text{SO}_4^{\cdot-}) = 2.01$ V) than $\text{SO}_4^{\cdot-}$ and $\cdot\text{OH}$ [16,17]. As can be observed from Fig. 7c, d and Fig. S4, all the time-profiled productions of $\text{S}_2\text{O}_8^{2-}$ exhibit the linear increase in the initial phase and gradually level off in the later stage. The highest $\text{S}_2\text{O}_8^{2-}$ concentration was obtained for the BTNAs anode at pH 3.0 during the 90 min electrolysis with the current efficiency of about 81.6% and 75.5% for $E_{\text{cell}} = 4.0$ and 2.5 V, respectively. The trends in $\text{S}_2\text{O}_8^{2-}$ accumulation and current efficiency indicate that solution pH and E_{cell} exerted the crucial effect on $\text{S}_2\text{O}_8^{2-}$ generation, which is associated closely with the generation mechanism of $\text{S}_2\text{O}_8^{2-}$. In general, the electrogeneration of $\text{S}_2\text{O}_8^{2-}$ at a non-active anode involves two steps [3,13,14] as described in Eq. (1)–(5). However, the results depicted in Fig. 4a and b state that the direct discharge of HSO_4^- on the β -PbO₂/TNAs and BTNAs anodes did not occur, which implies that $\cdot\text{OH}$ is the driving force for $\text{S}_2\text{O}_8^{2-}$ generation. Therefrom, the highest $\text{S}_2\text{O}_8^{2-}$ generation efficiency of BTNAs at pH = 3.0 and E_{cell}

= 4.0 V can be explained from the below aspects: (i) the low pH increasing the OER over-potential [30]; (ii) superior oxidizing ability of $\cdot\text{OH}$ in low pH media [6,28] along with efficient $\cdot\text{OH}$ -mediated oxidation of H_2SO_4 or HSO_4^- into $\text{SO}_4^{\cdot-}$; (iii) the negligible hydrolysis of $\text{SO}_4^{\cdot-}$ under acidic condition [9,17]. The change of pH with time under different initial pH values was also investigated. As shown in Fig. S5, the initial pH values of 9.0 and 12.0 changed to 3.8 ± 0.3 and 4.5 ± 0.4 at 90 min, respectively, due to OH^- consumption of the reactions Eqs. (12)–(14), indicating that the BTNAs anodes operated eventually under acidic conditions in divided cell containing bulk Na₂SO₄ electrolytes even at initial pH 9.0 and 12.0. While for the initial pH 3.0, only a small decline of the solution pH to 1.9 ± 0.2 was observed owing to the combined effect of Eqs. (4), (12), (15) and (16).



The enhanced $\cdot\text{OH}$ production from BTNAs anode may be ascribed to the bulk Ti^{3+} -induced high conductivity (as verified in EIS Nyquist curves) rather than Ti^{3+} acting as the active site [30,45], because the near-surface Ti^{3+} can be readily oxidized according to the XPS results. In fact, these observations can also be used to interpret the rapid descend in the RNO absorbance spectrum, which is certainly as a result of the collective effect of $\text{SO}_4^{\cdot-}$ and $\cdot\text{OH}$ originated from BTNAs anode.

The H₂O₂ accumulation performance on TNAs-N₂ cathode of BTNAs//TNAs-N₂ pair was also investigated. It can be clearly observed from Fig. 7e that the accumulated H₂O₂ experienced a linear growth in the first 30 min and then started to slowly increase during the 90 min bulk electrolysis in pH = 9.0 & 12.0 at $E_{\text{cell}} = 2.5$ V and pH = 3.0 at $E_{\text{cell}} = 4.0$ V. We speculate the reason may be the H₂O₂ decomposition side reaction caused by concentration accumulation in electrolyte. Compared with any other conditions, the highest cumulative H₂O₂ concentration and current efficiency of nearly 4.1 mM and 63.1% (Fig. 7e and f) were achieved at pH = 9.0, $E_{\text{cell}} = 2.5$ V, while the relatively lower accumulation and current efficiency were obtained under the conditions of pH = 3.0, $E_{\text{cell}} = 4.0$ V and pH = 12.0, $E_{\text{cell}} = 2.5$ V. Only a small amount of H₂O₂ accumulation was observed in the case of pH = 3.0, $E_{\text{cell}} = 2.5$ V, due to the slow electro-kinetics of 2e⁻-ORR. Moreover, nearly no H₂O₂ was produced for other two situations, which are probably caused by the further reduction and/or decomposition of the generated H₂O₂/HO₂⁻ (pK_a = 11.6 for H₂O₂ and approximately 70% of the generated H₂O₂ is in the form of HO₂⁻ at pH ≥ 12) [52, 53] at pH = 9.0 & 12.0, $E_{\text{cell}} = 4.0$ V, that is to say, the ORR switches from 2e⁻ to 4e⁻ route with the increasing overpotential. Above results are

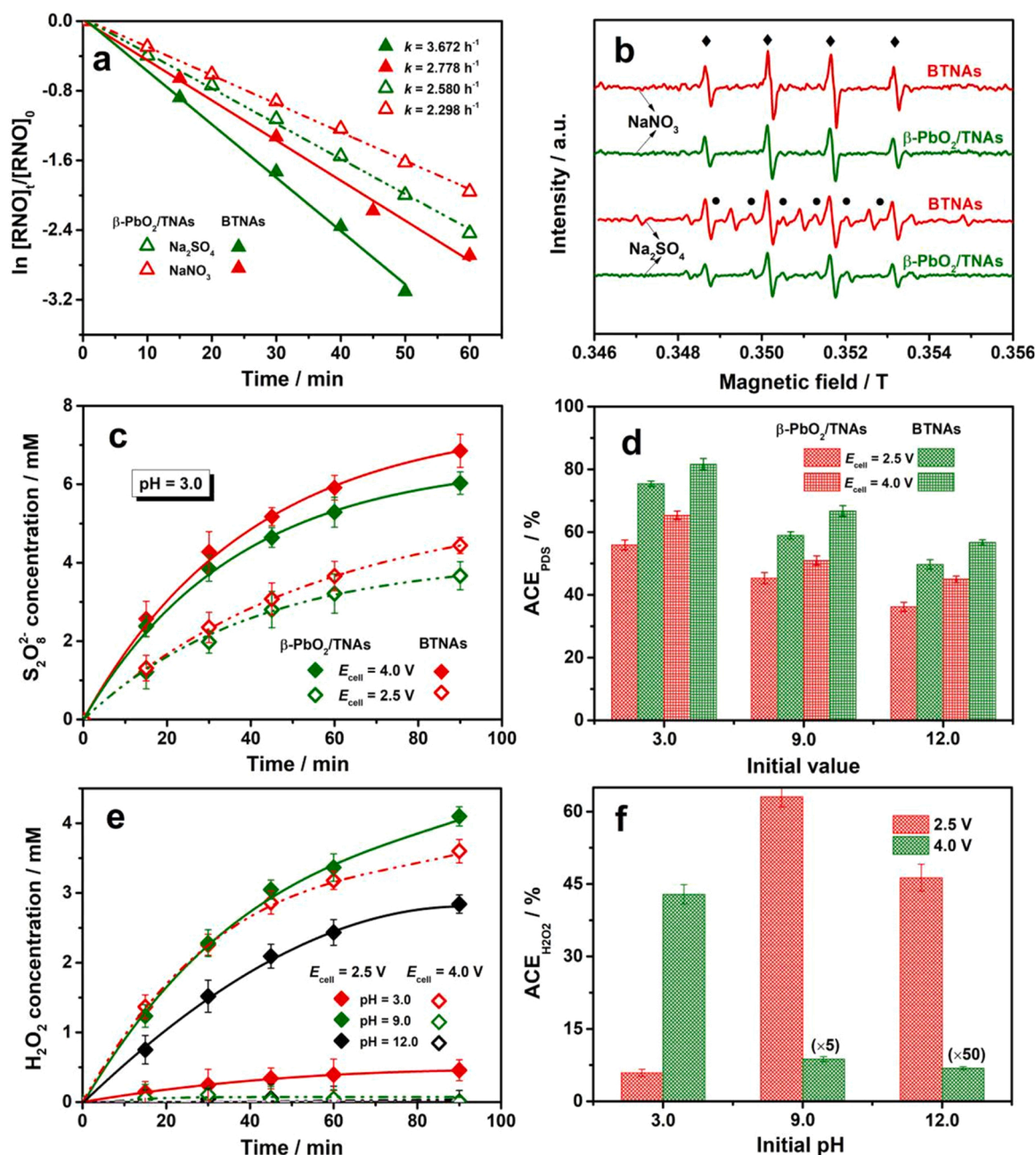


Fig. 7. (a) The kinetics analysis of RNO (20 μ M) bleaching by β -PbO₂/TNAs and BTNAs anodes in 0.1 M NaNO₃ and Na₂SO₄ electrolyte at $E_{\text{cell}} = 4.0 \text{ V}$ (data derived from Fig. S3), (b) The corresponding ESR spectra obtained by spin trapping with DMPO after 30 min electrolysis of β -PbO₂/TNAs and BTNAs anodes in 0.1 M Na₂SO₄ electrolyte (◆ and ● represent DMPO•OH and DMPO-SO₄^{•-} adducts, respectively). (c) S₂O₈²⁻ and (e) H₂O₂ accumulation in 0.1 M Na₂SO₄ electrolyte after 90 min electrolysis by using β -PbO₂/TNAs and BTNAs anodes and TNAs-N₂ cathode (BTNAs//TNAs-N₂ pair) at $E_{\text{cell}} = 2.5$ and 4.0 V , respectively. (d) and (f) show the corresponding average current efficiency, in which “ $\times 5$ ” and “ $\times 50$ ” represent the 5 and 50 times of ACE_{H₂O₂} value, respectively).

associated closely to the fact that solution pH and E_{cell} dominate the potential distribution of BTNAs//TNAs-N₂ pair, which endows TNAs-N₂ cathode different operating potential, causing different catalytic activity and electron transfer pathway of ORR, as confirmed by the results presented in Figs. 5 and 6. It should also be mentioned that when the accumulated H₂O₂ concentration is normalized into the amount produced per unit cathode area, the TNAs-N₂ cathode of BTNAs//TNAs-N₂ pair exhibits a comparable capacity to those reported in previous literature for H₂O₂ accumulation (Table S2), indicating their excellent electrocatalytic activities for H₂O₂/HO₂[•] production via 2e⁻-ORR, which is likely ascribed to: (i) the special nanotube arrays structure giving large surface area, and (ii) the high anatase crystalline degree increasing

conductivity and reactivity [34].

3.3.2. Berberine degradation in anode and cathode chambers

Berberine degradation was first performed in a divided cell as the reference experiment. Effects of the applied E_{cell} and initial pH on berberine decay in 0.1 M Na₂SO₄ electrolyte using β -PbO₂/TNAs and BTNAs anodes are depicted in Fig. 8a and b. It can be found that solution pH plays an important role on berberine removal efficiencies at given E_{cell} , and the fastest berberine degradation was achieved with BTNAs anode at initial pH = 3.0, $E_{\text{cell}} = 4.0 \text{ V}$. This fact is more evident in berberine color abatement presented in Fig. S6, which exhibits a total decolorization within only 40 min at pH 3.0. Furthermore, all decay

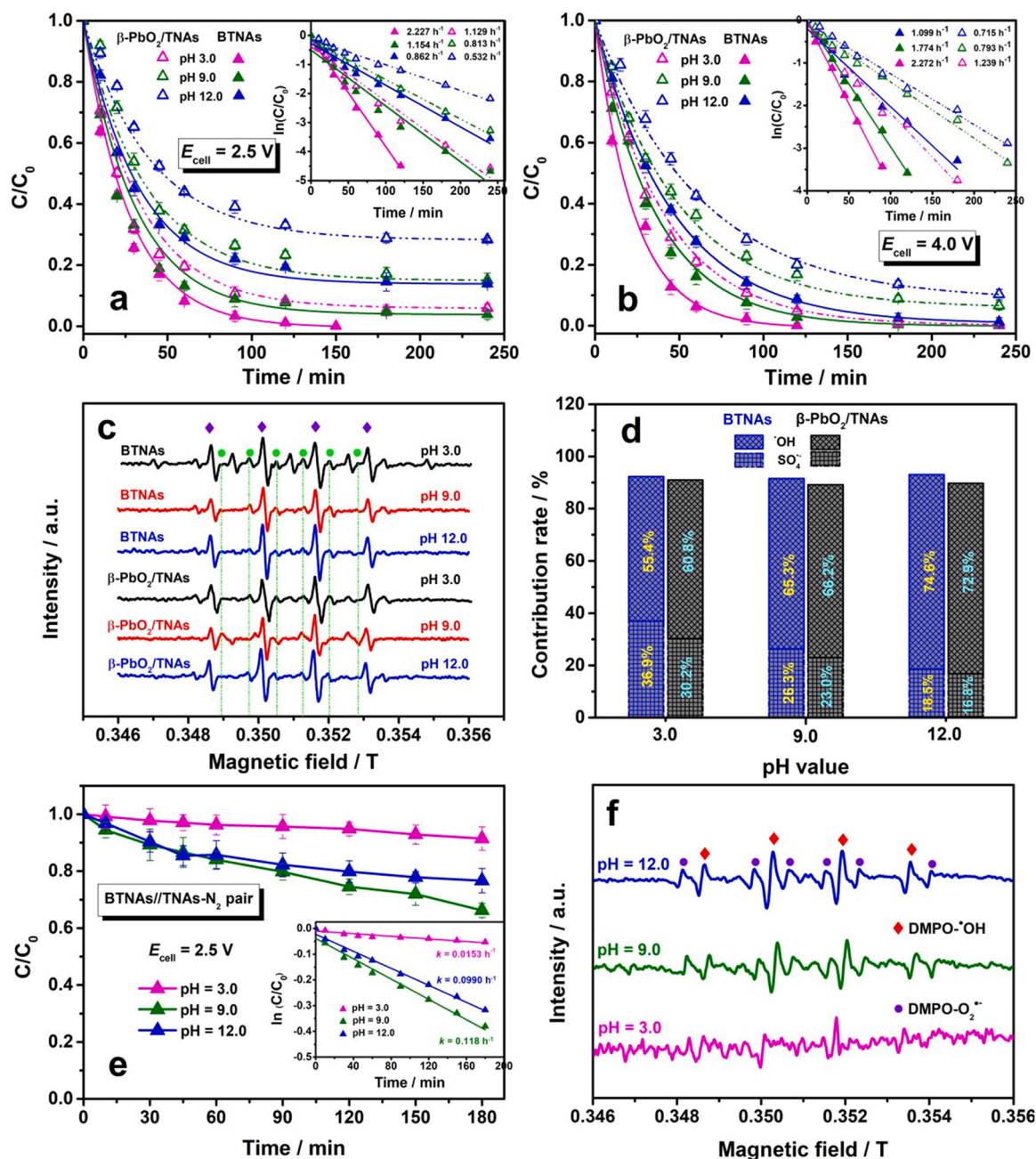


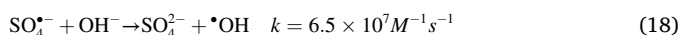
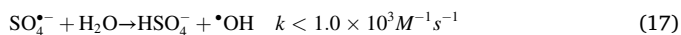
Fig. 8. Degradation profiles and kinetics analysis of berberine using β -PbO₂/TNAs and BTNAs anodes in different pH 0.1 M Na₂SO₄ electrolyte at E_{cell} of (a) 2.5 V and (b) 4.0 V, (c) ESR spectra obtained by spin trapping with DMPO after 30 min electrolysis of BTNAs and β -PbO₂/TNAs anodes at $E_{\text{cell}} = 4.0$ V (\blacklozenge and \bullet represent DMPO-•OH and DMPO-SO₄•- adducts, respectively), (d) The contribution of •OH and SO₄•- on berberine degradation by β -PbO₂/TNAs and BTNAs anodes in different pH 0.1 M Na₂SO₄ electrolytes at $E_{\text{cell}} = 4.0$ V (data derived from Table S3), (e) Berberine degradation in cathode chamber with BTNs//TNAs-N₂ pair in different pH 0.1 M Na₂SO₄ electrolyte at $E_{\text{cell}} = 2.5$ V, and (f) Corresponding ESR spectra of cathodically generated reactive oxygen species trapped by DMPO after 30 min electrolysis.

experiments follow the pseudo-first-order kinetics and the degradation rate constants on BTNAs are 1.5–2.2 folds of the ones obtained on β -PbO₂/TNAs. These results highlight the higher capability of BTNAs than that of β -PbO₂/TNAs for reactive radicals generation, and the berberine removal efficiencies are better at acidic pH. The ESR measurements presented in Fig. S7 also illustrated that more •OH radicals were produced in pH 3.0 NaNO₃ electrolyte, which is ascribed to the fact that lower pH is propitious to increase OER over-potential, boosting water oxidation into surface •OH, and in turn improving the electro-oxidation efficiency [16,30].

It is thoroughly established in the literature [13–17] that the

coexisting anions like SO₄²⁻ and HSO₄⁻ in sulfate solutions can evolve into SO₄•- under the actions of direct anodic oxidation and •OH chemical initiation (Eq. (1)–(4)). The ESR spectra shown in Fig. 8c provide a solid evidence for this fact, which display the characteristic signals of both DMPO-•OH and DMPO-SO₄•- adducts in Na₂SO₄ electrolyte, however, the strength of DMPO-•OH and DMPO-SO₄•- signals is different at different pH values. At pH 3.0, •OH has stronger oxidizing ability and can react with HSO₄⁻ to indirectly generate SO₄•-, attaining significantly higher electro-oxidation rates (Fig. 7b) due to their similar redox potential ($E^0(\text{SO}_4^{\bullet-}/\text{SO}_4^{2-}) = 2.5\text{--}3.1$ V vs. $E^0(\text{•OH}/\text{H}_2\text{O}) = 2.7$ V) and the negligible hydrolysis of SO₄•- under acidic condition (Eq. (17)) [9,17]. In

the case of pH 9.0, $\text{SO}_4^{\bullet-}$ is believed possessing the stronger reactivity than $\bullet\text{OH}$, but partial $\text{SO}_4^{\bullet-}$ can undergo hydrolysis to form $\bullet\text{OH}$ (Eq. (18)) [13,14], and meanwhile $\bullet\text{OH}$ can be consumed by OH^- [1,2,4], thereby the above superposition effects result in a decrease in $\text{SO}_4^{\bullet-}$ concentration.



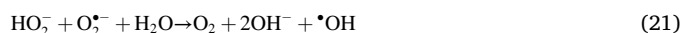
As a base reaction, the reactivity of $\text{SO}_4^{\bullet-}$ is less influenced by solution pH, however when the initial pH increases to 12.0, $\text{SO}_4^{\bullet-}$ will more easily combine with OH^- to generate $\bullet\text{OH}$, which has weaker oxidizability in this situation [2,16]. Accordingly, the removal efficiency of berberine under acidic condition is superior to that under alkaline condition, which is consistent with the results described in Fig. 8a and b.

Given that the reactivity of $\text{SO}_4^{\bullet-}$ is pH independent while that of $\bullet\text{OH}$ is pH dependent, it is hence necessary to investigate the responsible reactive radicals for berberine degradation using the quenching tests with the aid of selective chemical scavengers in different pH Na_2SO_4 electrolyte on the $\beta\text{-PbO}_2/\text{TNAs}$ and BTNAs anodes. As is widely known, the second-order rate constant of $\bullet\text{OH}$ with Ethanol (EtOH , $1.2\text{--}2.8 \times 10^9 \text{ M}^{-1} \text{ s}^{-1}$) and tert-Butanol (t-BuOH , $3.8\text{--}7.6 \times 10^8 \text{ M}^{-1} \text{ s}^{-1}$) is comparable, while $\text{SO}_4^{\bullet-}$ has a slower rate constant with t-BuOH ($4\text{--}9.1 \times 10^5 \text{ M}^{-1} \text{ s}^{-1}$) than that with EtOH ($1.6\text{--}7.7 \times 10^8 \text{ M}^{-1} \text{ s}^{-1}$) [2]. Therefore, t-BuOH mainly suppresses $\bullet\text{OH}$ and insensitive to $\text{SO}_4^{\bullet-}$, while EtOH is the scavenger for both the two type of reactive radicals. As displayed in Fig. S8, berberine degradation rate exhibits analogous inhibitory effect by adding 0.2 M t-BuOH and EtOH at pH 3.0, while a slightly increased inhibitory effect was achieved when t-BuOH concentration increases to 2.0 M, which indicates that 2.0 M t-BuOH is enough to effectively scavenge $\bullet\text{OH}$. Obviously, the berberine degradation is remarkably depressed after adding 2.0 M EtOH ($k = 0.171 \pm 0.03 \text{ h}^{-1}$) in comparison with adding 2.0 M t-BuOH ($k = 0.993 \pm 0.02 \text{ h}^{-1}$). This inhibition discrepancy between t-BuOH and EtOH scavengers can be ascribed to the indirectly generated $\text{SO}_4^{\bullet-}$ (Eqs. (3) and (4)), revealing that the collective effect of $\bullet\text{OH}/\text{SO}_4^{\bullet-}$ may responsible for berberine degradation, despite the generation of $\text{SO}_4^{\bullet-}$ will be restrained by scavenging $\bullet\text{OH}$ with the addition of t-BuOH [9,15].

The relative contribution of $\bullet\text{OH}$ and $\text{SO}_4^{\bullet-}$ in berberine degradation under different pH conditions can be roughly determined using the corresponding degradation rate constants of the radical inhibition tests that illustrated in Fig. S8 and Table S3. As shown in Fig. 8d, the relative contribution of $\bullet\text{OH}$ and $\text{SO}_4^{\bullet-}$ are calculated to be 60.8%, 30.2% and 55.4%, 36.9% for the $\beta\text{-PbO}_2/\text{TNAs}$ and BTNAs anodes at pH 3.0, respectively, suggesting that the $\bullet\text{OH}/\text{SO}_4^{\bullet-}$ joint-attack mechanism is responsible for the enhanced berberine removal under acidic condition, while the predominant active species is $\bullet\text{OH}$ for the two anodes in alkaline media. Above results can be interpreted by the following two aspects: (i) the efficient formation of $\bullet\text{OH}$ and $\text{SO}_4^{\bullet-}$ as well as the negligible hydrolysis of $\text{SO}_4^{\bullet-}$ (Eq. (17)) at pH 3.0; (ii) the conversion of $\text{SO}_4^{\bullet-}$ to $\bullet\text{OH}$ becomes prominent under alkaline conditions (Eq. (18)), namely, $\bullet\text{OH}$ generated from both water discharge and $\text{SO}_4^{\bullet-}$ hydrolysis plays a more critical role than $\text{SO}_4^{\bullet-}$, although the latter possesses better oxidative ability than $\bullet\text{OH}$ in this situation [2,16]. Notably, the sum of $\bullet\text{OH}$ and $\text{SO}_4^{\bullet-}$ contributions is less than 100%, which implies the involvement of other reactive species (not identified by ESR) in berberine degradation besides $\bullet\text{OH}$ and $\text{SO}_4^{\bullet-}$. Recent studies [11,35–37] have affirmed that non-radical reactive sulfate, i.e., $\text{S}_2\text{O}_8^{2-}$, which is partially responsible for organics degradation, may propagate during the electrochemical oxidation process in sulfate medium with the non-active anode. In present work, the direct electron transfer of berberine on $\beta\text{-PbO}_2/\text{TNAs}$ and BTNAs anode surfaces did not occur as depicted in Fig. 4a and b, however, the lower but non-negligible berberine degradation was still observed at both anodes in sulfate electrolyte during radical quenching tests (Fig. 8d and Fig. S8). This

result suggested that the persulfate's non-radical oxidation at anode may indeed exist and is responsible for berberine removal, as proposed by Song et al. [35–37].

Berberine degradation in cathode chamber containing different pH 0.1 M Na_2SO_4 solution was also investigated using $\text{BTNAs}/\text{TNAs-N}_2$ pair at $E_{\text{cell}} = 2.5 \text{ V}$ (Fig. 8e). Almost negligible berberine was removed when the electrolysis experiment was carried out at pH 3.0, whereas obvious degradation happened at pH 12.0 and pH 9.0 electrolytes. The maximum removal rate of ca. 32% was achieved at pH 9.0 with the pseudo-first-order rate constant of 0.118 h^{-1} , which is about 1.2 and 7.7 folds of that at pH 12.0 and 3.0, respectively. Above result may be closely associated with the generation of reactive radicals in cathode chamber. As shown in Fig. 8f, no significant $\text{DMPO-O}_2^{\bullet-}$ characteristic signals was observed at pH 3.0 even applying DMPO dissolved in methanol as spin-trapping agent, which is probably attributed to the facts: (i) $\text{O}_2^{\bullet-}$ is highly reactive and can associate with H^+ forming HO_2^{\bullet} [48,52], (ii) the low reaction rate of $\text{O}_2^{\bullet-}$ with DMPO ($k = 10\text{--}18 \text{ M}^{-1} \text{ s}^{-1}$). Unlike the acidic condition, the ESR spectra of pH 9.0 and 12.0 present the coupled signals of $\text{DMPO}\cdot\bullet\text{OH}$ and $\text{DMPO-O}_2^{\bullet-}$ adducts when adopting DMPO (dissolved in DI water) as spin-trapping agent, which is as a result of the enhanced stability of $\text{O}_2^{\bullet-}$ (about 1 min of lifespan) in alkaline pH (Eq. (19)), agreeing with the previous reports for $\text{O}_2^{\bullet-}$ and $\bullet\text{OH}$ detection [6,49]. Given that $\text{HO}_2^{\bullet}/\text{O}_2^{\bullet-}$ can not effectively oxidize organics relying on its limited redox potential (1.65 V) [48], above results validate that $\text{O}_2^{\bullet-}$ may indirectly account for the cathodic degradation of berberine through the further transformation into $\bullet\text{OH}$ ($\text{O}_2^{\bullet-} \rightarrow \text{HO}_2^{\bullet} \rightarrow \text{H}_2\text{O}_2/\text{HO}_2^- \rightarrow \bullet\text{OH}$) via the sustainable radical chain reactions (Eqs. (6)–(10)) and the Harber-Weiss reactions (Eqs. (20) and (21)), especially in alkaline media [5,9,54,55].



3.4. Berberine degradation and reactive radicals generation in an undivided cell

3.4.1. Berberine degradation

With regard to the electrochemical degradation of organics, the previous studies have basically focused on anodic oxidation while the cathodic reactions are often ignored. Nevertheless, many literature have experimentally corroborated that the degradation rate of organic contaminants can be efficiently enhanced in an undivided cell using a non-active anode and an active cathode [41,42,56,57]. The plots of berberine concentration and corresponding TOC changes over time during berberine degradation in an undivided cell with $\text{BTNAs}/\text{TNAs-N}_2$ pair at the different pH and E_{cell} are depicted in Fig. 9a and c. In all cases, the similar trends in berberine and its TOC decay were found under the identical condition. The fastest berberine removal was achieved at pH = 3.0, $E_{\text{cell}} = 4.0 \text{ V}$ after ca. 120 min electrolysis with the pseudo-first-order rate constant of 2.855 h^{-1} , which is approximately 1.3 times as high as that of the BTNAs anode in a divided cell, as shown in Fig. 8b. Besides, about 49.3% mineralization was also reached at this condition, whereas only 29.8% mineralization was obtained at pH = 12.0, $E_{\text{cell}} = 2.5 \text{ V}$ after 360 min of electrolysis. The analogous TOC abatement tendency was also observed for the BTNAs anode in the divided cell (Fig. 9d), with the apparently depressed mineralization rate of 44.2% and 25.4% at pH = 3.0, $E_{\text{cell}} = 4.0 \text{ V}$ and pH = 12.0, $E_{\text{cell}} = 2.5 \text{ V}$, respectively. Above findings provide strong experimental evidence for the strong impact of TNAs-N_2 cathode on berberine degradation in the undivided cell.

For both reactor configuration, the corresponding MCE values obtained at given E_{cell} dropped gradually with the sequence of pH 3.0 > pH 9.0 > pH 12.0 as the electrolysis proceeds. Normally, a higher MCE

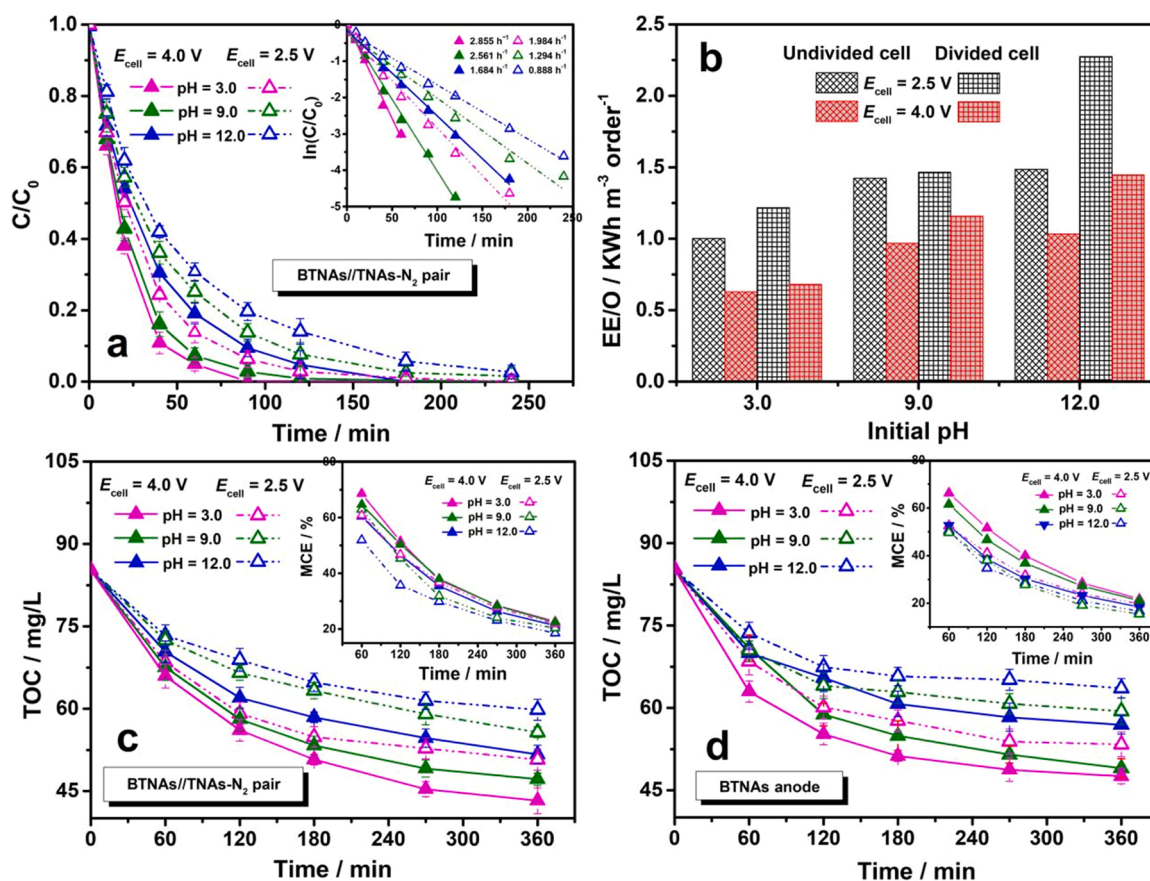


Fig. 9. (a) Degradation profiles and kinetics analysis of berberine using BTNAs//TNAs-N₂ pair in different pH O₂-saturated 0.1 M Na₂SO₄ electrolyte at $E_{\text{cell}} = 2.5$ V and 4.0 V, (b), (c) and (d) electrical energy per order of magnitude and TOC abatement with electrolysis time during berberine degradation performed in the divided and undivided cells at different pH and E_{cell} , respectively. The insets of (c) and (d) show the corresponding mineralization current efficiency.

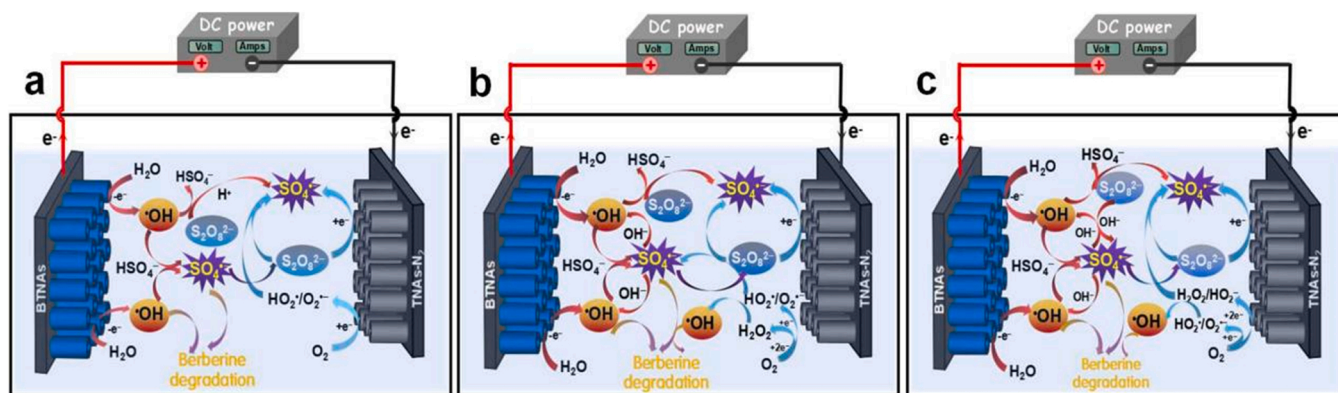
value is correlated with the stronger oxidation power of the specific degradation system [6,42]. As for the most powerful treatment process in present work, i.e., BTNAs//TNAs-N₂ pair in an undivided cell at pH = 3.0 and $E_{\text{cell}} = 4.0$ V, the MCE decreases from 68.6% at 60 min to 22.7% at 360 min. In the light of no undesirable side reactions such as oxygen evolution at BTNAs anode and hydrogen evolution at TNAs-N₂ cathode occurred, the gradually reduced MCE can be attributed to the gradual reduction of the easily-degraded organics and the gradual accumulation of more recalcitrant intermediates during degradation process. Similar situations were also found for BTNAs anode in a divided cell under the same condition, because of generating quite analogous or identical intermediates during the treatments [1].

EE/O and EC_{TOC} are two important parameters to comprehensively assess the energy efficiency and economic viability of EAOPs in practical applications [23,30,42]. It can be clearly seen from Fig. 9b and Table S4 that the highest and lowest EE/O and EC_{TOC} values of BTNAs//TNAs-N₂ pair in the undivided cells and BTNAs anode in the divided cells were both achieved at pH = 12.0, $E_{\text{cell}} = 2.5$ V and pH = 3.0, $E_{\text{cell}} = 4.0$ V, respectively. This means that the energy consumption for berberine degradation and corresponding TOC abatement increase with pH under the same reactor configuration and E_{cell} , which is an opposite trend to MCE, further confirming that electrolyte pH directly dominates the reaction kinetics of berberine with the electro-generated reactive radicals. Aforementioned different berberine degradation and energy consumption behaviors under different operating condition can be associated with the pH-induced different oxidation ability: (i) with regard to the low-oxidative ability process, more time was required to generate adequate reactive radicals for berberine degradation per order of magnitude and TOC decay, whereas (ii) with respect to the

high-oxidative ability process, the generated refractory intermediates would compete reactive radicals with the easily-degraded intermediates and berberine. Based on the above results, no matter experiments proceeding in the undivided or divided cells the BTNAs is always an efficient anode for berberine degradation within a wide pH range. Meanwhile, the TNAs-N₂ cathode plays an important role on the co-generation of reactive radicals in an undivided cell. Therefore, the mechanism of reactive radicals co-generation in an undivided cell under different pH and E_{cell} should be investigated comprehensively.

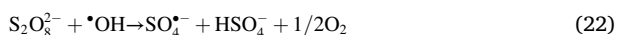
3.4.2. Reactive radicals generation mechanism

Solution pH is an important variable in EAOPs and plays a crucial role on organic contaminants degradation by tuning reactive radicals production mechanism, due to the participation of protons in many radical chain reactions [1,5,30]. In present work, electrolyte pH mainly dominates E_c distribution and affects ORR pathway as depicted in Fig. 6. Therefore, the cathodically formed reactive oxygen species, such as $O_2^{\bullet-}/HO_2^{\bullet}$ and H_2O_2/HO_2^{\bullet} , are bound to involve in sulfate activation and reactive radicals generation processes, resulting in the accelerated berberine degradation through a multi-radical joint-attack mechanism. In this context, the insight into the role of cathodic ORR on the enhanced berberine degradation was needed to be deeply analyzed. In common, the different quantities of $SO_4^{\bullet-}$ and $S_2O_8^{\bullet-}$ would generate via Eqs. (3)–(5) with $\bullet OH$ as the predominant precursor in BTNAs anode area. Based on this, the possible mechanism of pH-dependent reactive radicals co-generation in an undivided cell with BTNAs//TNAs-N₂ pair was summarized in Scheme 2 (Taking $E_{\text{cell}} = 2.5$ V for example).



Scheme 2. Schematic diagrams of reactive radicals co-generation mechanism in an undivided cell containing different pH O₂-saturated 0.1 M Na₂SO₄ electrolyte using BTNAs//TNAs-N₂ pair at: (a) pH 3.0, (b) pH 9.0 and (c) pH 12.0.

- i) At pH 3.0, the lower pH value is beneficial to increase the oxygen overpotential of BTNAs anode, which can effectively depress the oxygen evolution side reaction (Eq. (12)), thereby producing more SO₄•⁻ and S₂O₈²⁻. The generated S₂O₈²⁻ can also be activated by •OH (Eq. (22)) or TNAs-N₂ cathode (Eq. (23)) to produce SO₄•⁻, and meanwhile S₂O₈²⁻ would continuously be regenerated through Eqs. (3)–(5), thereby establishing an ideal S₂O₈²⁻ → SO₄•⁻ → S₂O₈²⁻ shuttle cycle [3,6,13].



In this condition, the ORR products are mainly HO₂•, because

the slow electro-kinetics of TNAs-N₂ cathode can not sufficiently driven the further one-electron reduction of O₂•⁻ to generate massive H₂O₂ (Eq. (9)), as illustrated in Fig. 6. The relative low redox potential of HO₂• is incompetent for effective oxidative degradation of organic pollutants, but fortunately, HO₂• can efficiently activate S₂O₈²⁻ forming SO₄•⁻ via Eq. (24) with the rate constant about 10-fold higher than that of O₂•⁻ (Eq. (25)) [5]. Undoubtedly, this is a more efficient S₂O₈²⁻ activation pathway for SO₄•⁻ generation than by cathodic activation (Eq. (23)), owing to the electrostatic repulsive effect between S₂O₈²⁻ and TNAs-N₂ cathode. Besides, the conversion of SO₄•⁻ into •OH through Eq. (18) is inconspicuous in this condition, due to its lower rate constant than that of the oxidative degradation reaction of SO₄•⁻. Consequently, the aforementioned synergistic activation

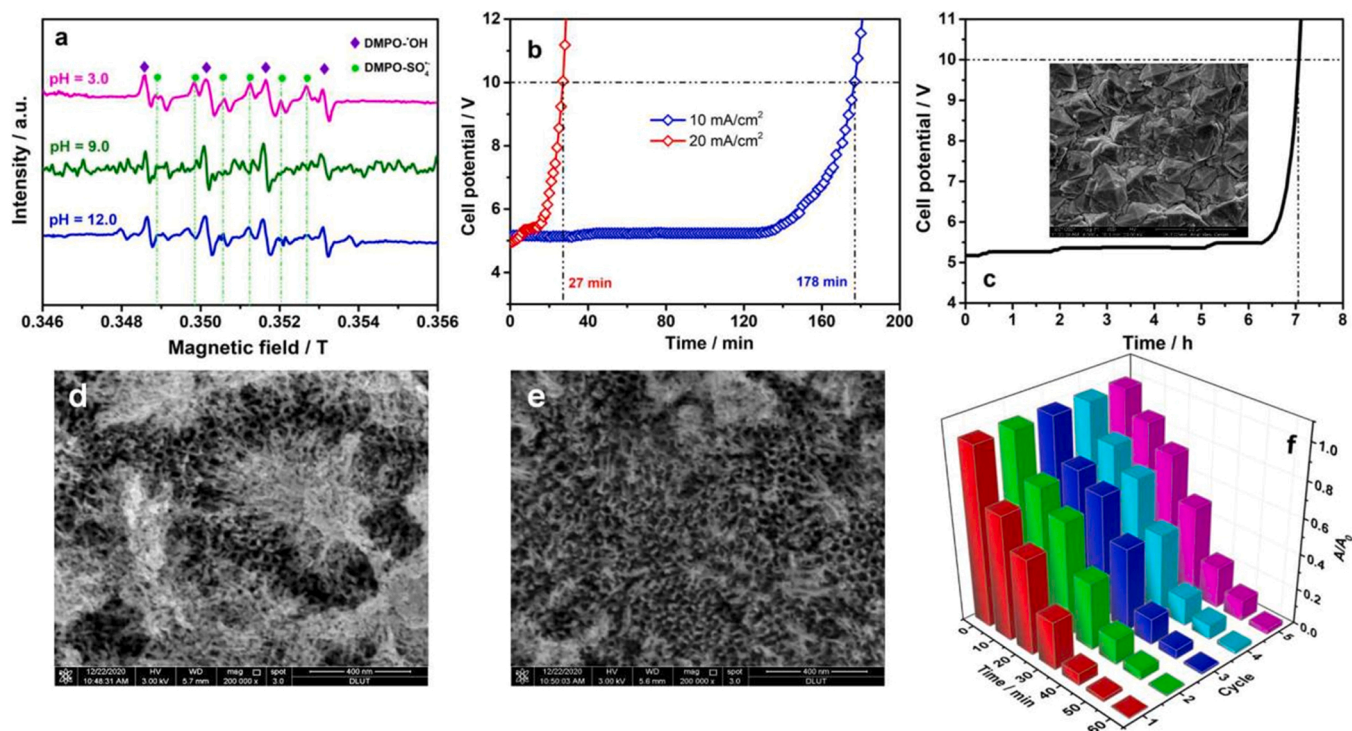
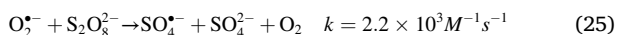
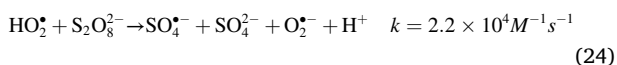


Fig. 10. (a) ESR spectra obtained by spin trapping with DMPO after 30 min electrolysis of BTNAs //TNAs-N₂ pair in an undivided cell containing different pH 0.1 M Na₂SO₄ electrolyte at $E_{\text{cell}} = 2.5$ V. The accelerated life tests on (b) BTNAs electrode at 10 and 20 mA/cm² and (c) β-PbO₂/TNAs electrode at 1.0 A/cm² in 1.0 M H₂SO₄ electrolyte, respectively. The inset of (c) and (d) show the SEM images of β-PbO₂/TNAs and BTNAs electrodes after accelerated life tests, respectively, (e) the SEM image of the deactivated BTNAs electrode after cathodic polarization treatment. (f) five consecutive cycles (1.0 h per cycle) of berberine decolorization by the regenerated BTNAs anode in a divided cell containing pH 3.0, 0.1 M Na₂SO₄ electrolyte at $E_{\text{cell}} = 4.0$ V.

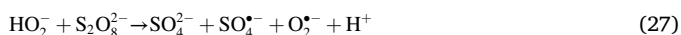
processes achieves a $\text{SO}_4^{\bullet-}$ -dominated $\cdot\text{OH}/\text{SO}_4^{\bullet-}$ collective degradation mechanism (Fig. 10a).



- ii) At pH 9.0, the TNAs- N_2 cathode could efficiently catalyze 2e^- -ORR forming H_2O_2 , but the increased pH would reduce the overpotential of oxygen evolution side reaction, thus affecting $\cdot\text{OH}$, $\text{SO}_4^{\bullet-}$ and $\text{S}_2\text{O}_8^{2-}$ yields of BTNAs anode. Apart from reactions of Eqs. (24) and (25), another effective activation route of $\text{S}_2\text{O}_8^{2-}$ would develop via Eq. (26) with H_2O_2 as an activator [42]. However, the generated $\text{SO}_4^{\bullet-}$ tends to convert into $\cdot\text{OH}$ by reacting with OH^- ions via Eq. (18), and moreover the interaction between H_2O_2 and $\text{O}_2^{\bullet-}$ will benefit to yield $\cdot\text{OH}$ via Eq. (20). Above processes significantly reduced $\text{SO}_4^{\bullet-}$ accumulation (Fig. 9a), and hence weakened the contribution of $\text{SO}_4^{\bullet-}$ for berberine degradation.



- iii) At pH 12.0, the stability of $\text{O}_2^{\bullet-}$ are significantly enhanced due to the obvious decrease of proton transfer rate in electrolyte. Then, $\cdot\text{OH}$, $\text{O}_2^{\bullet-}$ and $\text{H}_2\text{O}_2/\text{HO}_2^-$ originated respectively from anodic and cathodic areas could further activate $\text{S}_2\text{O}_8^{2-}$ to produce $\text{SO}_4^{\bullet-}$ through Eqs. (22) and (24)-(27)) [5].



On the other hand, it is generally believed that $\text{S}_2\text{O}_8^{2-}$ is highly reactive under strong alkaline conditions, thus the base activation mechanism of $\text{S}_2\text{O}_8^{2-}$ via Eq. (13) [53] is not negligible at pH = 12.0. Nevertheless, the transformation of $\text{SO}_4^{\bullet-}$ to $\cdot\text{OH}$ via Eq. (18) would become more prominent in a strong alkaline electrolyte (pH > 10.5) [5, 9,55]. Above processes created a $\cdot\text{OH}$ -dominated $\cdot\text{OH}/\text{SO}_4^{\bullet-}$ collective degradation mechanism (Fig. 9a). The relative low redox potential of $\cdot\text{OH}$ at high pH resulted in low TOC removal efficiency and high energy consumption.

In summary, the electrolyte pH plays a very crucial role in the generation of $\cdot\text{OH}$, $\text{SO}_4^{\bullet-}$ and $\text{S}_2\text{O}_8^{2-}$ near BTNAs anode surface as well as ORR pathway or products in TNAs- N_2 cathode area, which consequently dominates the following reaction processes: the activation of $\text{S}_2\text{O}_8^{2-}$, the conversion of $\text{SO}_4^{\bullet-}$ to $\cdot\text{OH}$, and the interaction between $\text{H}_2\text{O}_2/\text{HO}_2^-$ and $\text{O}_2^{\bullet-}/\text{HO}_2^-$ for $\cdot\text{OH}$ generation, resulting in the pH-dependent ORR-strengthened synergistic sulfate activation process with the multi-radical co-generation and joint-attack mechanism.

3.4.3. Accelerated service lifetime tests

The stability and reusability of BTNAs electrode are the most important factors for their practical applications in EAOPs wastewater treatment, being expected a longer service lifetime in the strong acidic media under a large current density [10,28]. As shown in Fig. 10b, the accelerated life of BTNAs electrode is about 178 and 27 min at 10 and 20 mA/cm^2 , respectively, and then the n value was determined by Eq. (S10) to be ca. 2.72. Thus, the actual service lifetime of BTNAs electrode operating at 3.24 and 4.0 mA/cm^2 (corresponding to $E_{\text{cell}} = 2.5$ V and 4.0 V, as displayed in Fig. S9a) was about 64 and 36 h, respectively.

In fact, above tests performed at low current densities are not the real accelerated life measurements. It is also impossible for us to perform the accelerated lifetime test on BTNAs electrode at a high current density of 1.0 A/cm^2 , since a high anode potential far beyond 10 V would achieve rapidly (data not shown). However, the accelerated life test for $\beta\text{-PbO}_2$ /

TNAs under the same condition is approximately 7 h (Fig. 10c). In contrast to the corrosion and morphology damage of BTNAs (Fig. 10d), only slight cracks and stripping of $\beta\text{-PbO}_2$ coating were observed on $\beta\text{-PbO}_2$ /TNAs electrode (inset of Fig. 10c). This extended service lifetime of $\beta\text{-PbO}_2$ /TNAs electrode can be ascribed to the facts: i) the short-time electrochemically reduced TNAs interlayer strengthens the adhesion of $\beta\text{-PbO}_2$ coating, as a result preventing its peel-off, ii) the uniform and compact $\beta\text{-PbO}_2$ coating can effectively inhibits electrolyte and active oxygen infiltration into Ti/TNAs matrix, leading to good corrosion resistance.

Although the low service lifetime of the BTNAs electrode is anyhow inapplicable for the actual industrial application, Cai et al. [10] affirmed that the deactivated BTNAs electrodes can be renewed to nearly original performance via the electrochemical re-reduction treatment. Similar result was also obtained in this work after we dealt with the deactivated BTNAs by cathodic polarization in 10% formic acid solution at a current density of 10 mA/cm^2 for 20 min. As seen from Fig. 10e, the relatively regular nanotube array morphology was mostly recovered after cathodic polarization, and the oxygen evolution potential decreases slightly but can still reach at ca. 2.56 V vs Ag/AgCl (Fig. S9b). Five consecutive cycles of berberine decolorization trials that conducted in a divided cell at pH = 3.0, $E_{\text{cell}} = 4.0$ V (Fig. 10f) exhibit stable color removal performance, and the chroma decay efficiency in the last test is still 93.2% of that in the first test, indicating the comparable electro-oxidation ability of the regenerated BTNAs anode with the fresh one, due to Ti^{3+} re-formation [28] and its electro-activity recovery after cathodic polarization.

3.5. Proposed degradation pathways of Berberine

The degradation intermediates of berberine were determined by LC-MS and the corresponding chromatographic spectra and their mass-to-charge (m/z) values of these identified intermediates are illustrated in Fig. S10 and Fig. S11. As seen, the intensity of berberine characteristic peak (336 m/z) decreases with the increase of electrolysis time. Based on the corresponding m/z values in MS patterns, three possible pathways of berberine removal during the single-chamber electrolysis treatment using BTNAs//TNAs- N_2 pair at $E_{\text{cell}} = 4.0$ V were proposed in Fig. 11. Ordinarily, the homogeneous $\text{SO}_4^{\bullet-}$ tends to react with organic compounds primarily through direct electron transfer, while $\cdot\text{OH}$ prefers to H-abstraction and unsaturated bonds addition reactions [8,13]. First, under the oxidative attacks of $\cdot\text{OH}/\text{SO}_4^{\bullet-}$, the cleavage of the most susceptible sites in berberine molecule, i.e., pyridine ring and lateral dimethoxymethane group ($-\text{O}-\text{CH}_2-\text{O}-$), generates two isomers (338 m/z) [58,59], C1 and C2. Simultaneously, the demethylation process and the electron transfer between $\text{SO}_4^{\bullet-}$ and berberine produce C3 (323 m/z) [41,58]. In pathway one: the C1 undergoes $-\text{OCH}_2\text{O}-$ splitting and demethylation forming C4 (311 m/z) [60], followed by the dehydroxylation, ring-opening and ring-refactoring reactions generating C5 (283 m/z), and then the later is transformed into C6 (133 m/z), C7 (200 m/z) and C9 (166 m/z) via the oxidative bond-breaking. In pathway two: the consecutive pyridine ring-opening of C2 leads to the formation of C8 (280 m/z) and C9. Afterwards, the C7 and C9 can be further oxidized as to lose methyl and ethyl groups forming C10 (124 m/z), which is responsible for the formation of C14 (123 m/z). In pathway three: the ring-opening and ring-refactoring of C3 leads to the formation of C11 (279 m/z), which can be further oxidative transformed to C6 and C12 (183 m/z) via simultaneous pyridine ring-opening, $-\text{O}-\text{CH}_2-\text{O}-$ cleavage and hydroxylation reactions [58–60]. The C12 experienced dehydroxylation, demethylation and acidization processes forming C13 (151 m/z) and (14). In addition, the further oxidation of C6 produces C15 (84 m/z) via pyridine ring-opening reaction. Finally, the intermediates C10, C14 and C15 will be partially mineralized to carbon dioxide, water and nitrate ion through the organic by-products, such as formic acid and acetic acid [1,61].

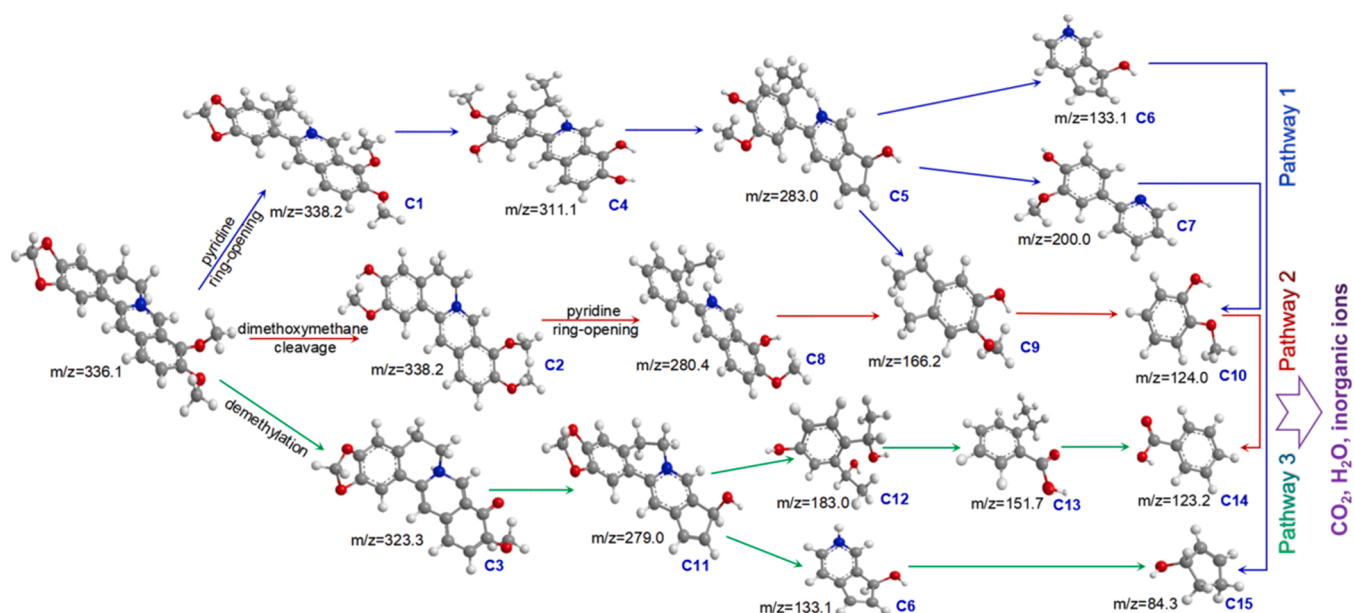


Fig. 11. The proposed degradation pathway of berberine by BTNAs//TNAs-N₂ pair at $E_{\text{cell}} = 4.0$ V in an undivided cell containing pH 3.0, O₂-saturated 0.1 M Na₂SO₄ electrolyte.

4. Conclusions

This work reports a systematic study on the sulfate electro-activation behavior and mechanisms in the divided and undivided cells by a novel anodic oxidation-cathodic ORR coupled system using the TNAs-based electrodes. In double-chamber reactor, both β -PbO₂/TNAs and BTNAs anodes possess high oxygen evolution potential and low charge transfer resistance, while the applied E_{cell} , electrolyte type and pH dominate anodic sulfate activation, reactive radical formation and TNAs-N₂ cathodic ORR performance. Although the oxidation behavior and radical generation mechanism in the anodic and cathodic half-reactions are entirely different, the higher oxidation power is obtained in the single-chamber reactor, which is attributed to the synergistic effect originated from the individual anodic oxidation and cathodic ORR processes for the efficient co-generation of $\cdot\text{OH}$ and $\text{SO}_4^{\cdot-}$, resulting in satisfactory degradation/mineralization kinetics and energy cost. Apart from H₂O₂, the O₂ $^{\cdot-}$, HO₂ $^{\cdot}$ and HO₂ $^{\cdot}$ formed from the pH-dependant ORR process play beneficial roles and serve as important activators in sulfate electro-activation process. The degradation pathway of berberine mainly involves -OCH₂O- bond cleaving, pyridine and other aromatic ring-opening reactions initiated by the joint-attack of $\cdot\text{OH}/\text{SO}_4^{\cdot-}$ (the contribution of O₂ $^{\cdot-}/\text{HO}_2^{\cdot}$ is minor). Overall, this pH-dependent ORR-strengthened synergistic sulfate activation process will be a viable candidate for EAOPs treatment of sulfate-containing refractory organics wastewater.

CRediT authorship contribution statement

Guoquan Zhang: Conceptualization, Methodology, Writing – original draft, Writing – review & editing, Supervision. **Luying Zhao:** Investigation, Data curation, Validation, Writing – original draft, Writing – review & editing. **Xiaoxin Hu:** Investigation, Data curation, Validation, Writing – original draft, Writing – review & editing. **Xiaoyu Zhu:** Investigation, Data curation, Validation. **Fenglin Yang:** Project administration.

Declaration of Competing Interest

The authors declare that they have no known competing financial interests or personal relationships that could have appeared to influence

the work reported in this paper.

Acknowledgements

This work was financially supported by the National Natural Science Foundation of China (No. 21437001) and the Programme of Introducing Talents of Discipline to Universities (No. B13012).

Appendix A. Supporting information

Supplementary data associated with this article can be found in the online version at [doi:10.1016/j.apcatb.2022.121453](https://doi.org/10.1016/j.apcatb.2022.121453).

References

- [1] E. Brillas, I. Sires, M.A. Oturan, Electro-Fenton process and related electrochemical technologies based on Fenton's reaction chemistry, *Chem. Rev.* 109 (2009) 6570–6631, <https://doi.org/10.1021/cr900136g>.
- [2] W.-D. Oh, Z. Dong, T.-T. Lim, Generation of sulfate radical through heterogeneous catalysis for organic contaminants removal: current development, challenges and prospects, *Appl. Catal. B: Environ.* 194 (2016) 169–201, <https://doi.org/10.1016/j.apcatb.2016.04.003>.
- [3] J. Radjenovic, D.L. Sedlak, Challenges and opportunities for electrochemical processes as next generation technologies for the treatment of contaminated water, *Environ. Sci. Technol.* 49 (2015) 11292–11302, <https://doi.org/10.1021/acs.est.5b02414>.
- [4] S.O. Ganiyu, C.A. Martínez-Huitle, Nature, Mechanisms and Reactivity of Electrogenated Reactive Species at Thin-Film Boron-Doped Diamond (BDD) Electrodes During Electrochemical Wastewater Treatment, *ChemElectroChem* 6 (2019) 2379–2392, <https://doi.org/10.1002/celec.201900159>.
- [5] P. Devi, U. Das, A.K. Dalai, In-situ chemical oxidation: principle and applications of peroxide and persulfate treatments in wastewater systems, *Sci. Total Environ.* 571 (2016) 643–657, <https://doi.org/10.1016/j.scitotenv.2016.07.032>.
- [6] S.O. Ganiyu, C.A. Martínez-Huitle, M.A. Oturan, Electrochemical advanced oxidation processes for wastewater treatment: advances in formation and detection of reactive species and mechanisms, *Curr. Opin. Electrochem.* 27 (2021), 100678, <https://doi.org/10.1016/j.coelec.2020.100678>.
- [7] J.E.L. Santos, M.A. Quiroz, M. Cerro-Lopez, D.C. de Moura, C.A. Martínez-Huitle, Evidence for the electrochemical production of persulfate at TiO₂ nanotubes decorated with PbO₂, *N. J. Chem.* 42 (2018) 5523–5531, <https://doi.org/10.1039/C7NJ02604H>.
- [8] G.G. Bessegato, M.V.B. Zanoni, G. Tremiliosi-Filho, C.A. Lindino, Evidences of the electrochemical production of sulfate radicals at cathodically polarized TiO₂ nanotubes electrodes, *Electrochim. Acta* 10 (2019) 272–276, <https://doi.org/10.1007/s12678-019-00525-6>.
- [9] L. Chen, C. Lei, Z. Li, B. Yang, X. Zhang, L. Lei, Electrochemical activation of sulfate by BDD anode in basic medium for efficient removal of organic pollutants,

- Chemosphere 210 (2018) 516–523, <https://doi.org/10.1016/j.chemosphere.2018.07.043>.
- [10] J. Cai, M. Zhou, Y. Pan, X. Du, X. Lu, Extremely efficient electrochemical degradation of organic pollutants with co-generation of hydroxyl and sulfate radicals on Blue-TiO₂ nanotubes anode, *Appl. Catal. B: Environ.* 257 (2019), 117902, <https://doi.org/10.1016/j.apcatb.2019.117902>.
 - [11] S.O. Ganiyu, M.G. El-Din, Insight into in-situ radical and non-radical oxidative degradation of organic compounds in complex real matrix during electrooxidation with boron doped diamond electrode: a case study of oil sands process water treatment, *Appl. Catal. B Environ.* 279 (2020), 119366, <https://doi.org/10.1016/j.apcatb.2020.119366>.
 - [12] J.E.L. Santos, D.R. da Silva, C.A. Martínez-Huitle, E.V. dos Santos, M.A. Quiroz, Cathodic hydrogen production by simultaneous oxidation of methyl red and 2,4-dichlorophenoxyacetate aqueous solutions using Pb/PbO₂, Ti/Sb-doped SnO₂ and Si/BDD anodes. Part 1: electrochemical oxidation, *RSC Adv.* 10 (2020) 37695–37706, <https://doi.org/10.1039/D0RA03955A>.
 - [13] A. Farhat, J. Keller, S. Tait, J. Radjenovic, Removal of persistent organic contaminants by electrochemically activated sulfate, *Environ. Sci. Technol.* 49 (2015) 14326–14333, <https://doi.org/10.1021/acs.est.5b02705>.
 - [14] Y.-U. Shin, H.-Y. Yoo, Y.-Y. Ahn, M.S. Kim, K. Lee, S. Yu, C. Lee, K. Cho, H. Kim, J. Lee, Electrochemical oxidation of organics in sulfate solutions on boron-doped diamond electrode: Multiple pathways for sulfate radical generation, *Appl. Catal. B Environ.* 254 (2019) 156–165, <https://doi.org/10.1016/j.apcatb.2019.04.060>.
 - [15] J. Ding, L. Bu, Q. Zhao, F.T. Kabutye, L. Wei, D.D. Dionysiou, Electrochemical activation of persulfate on BDD and DSA anodes: electrolyte influence, kinetics and mechanisms in the degradation of bisphenol A, *J. Hazard. Mater.* 388 (2020), 121789, <https://doi.org/10.1016/j.jhazmat.2019.121789>.
 - [16] X. Duan, C. Su, L. Zhou, H. Sun, A. Zhavorov, T. Odedairo, Z. Zhu, Z. Shao, S. Wang, Surface controlled generation of reactive radicals from persulfate by carbocatalysis on nanodiamonds, *Appl. Catal. B Environ.* 194 (2016) 7–15, <https://doi.org/10.1016/j.apcatb.2016.04.043>.
 - [17] J. Davis, J.C. Baygents, J. Farrell, Understanding persulfate production at boron doped diamond film anodes, *Electrochim. Acta* 150 (2014) 68–74, <https://doi.org/10.1016/j.electacta.2014.10.104>.
 - [18] L.W. Matzek, M.J. Tipton, A.T. Farmer, A.D. Steen, K.E. Carter, Understanding electrochemically activated persulfate and its application to ciprofloxacin abatement, *Environ. Sci. Technol.* 52 (2018) 5875–5883, <https://doi.org/10.1021/acs.est.8b00015>.
 - [19] Z. Wang, Y. Mao, M. Xu, Y. Wei, Y. Hu, C. Zhu, W. Fang, F. Wang, Fabrication and enhanced electrocatalytic activity of three-dimensional sphere-stacking PbO₂ coatings based on TiO₂ nanotube arrays substrate for the electrochemical oxidation of organic pollutants, *J. Electrochem. Soc.* 164 (2017) H981–H988, <https://doi.org/10.1149/2.0151714jes>.
 - [20] J.E.L. Santos, D.C. de Moura, D.R. da Silva, M. Panizza, C.A. Martínez-Huitle, Application of TiO₂-nanotubes/PbO₂ as an anode for the electrochemical elimination of Acid Red 1 dye, *J. Solid State Electrochem.* 23 (2019) 351–360, <https://doi.org/10.1007/s10008-018-4134-5>.
 - [21] C. Yang, S. Shang, X. Li, Fabrication of sulfur-doped TiO₂ nanotube array as a conductive interlayer of PbO₂ anode for efficient electrochemical oxidation of organic pollutants, *Sep. Purif. Technol.* 258 (2021), 118035, <https://doi.org/10.1016/j.seppur.2020.118035>.
 - [22] J. Lyu, G. Sun, L. Zhu, H. Ma, C. Ma, X. Dong, Y. Fu, Fabrication of Ti/black TiO₂-PbO₂ micro/nanostructures with tunable hydrophobic/hydrophilic characteristics and their photoelectrocatalytic performance, *J. Solid State Electrochem.* 24 (2020) 375–387, <https://doi.org/10.1007/s10008-019-04433-z>.
 - [23] X. Meng, Z. Chen, C. Wang, W. Zhang, K. Zhang, S. Zhou, J. Luo, N. Liu, D. Zhou, D. Li, J. Crittenden, Development of a three-dimensional electrochemical system using a blue TiO₂/SnO₂-Sb₂O₃ anode for treating low-ionic-strength wastewater, *Environ. Sci. Technol.* 53 (2019) 13784–13793, <https://doi.org/10.1021/acs.est.9b05488>.
 - [24] A. Ansari, D. Nematollahi, Convergent paired electrocatalytic degradation of p-dinitrobenzene by Ti/SnO₂-Sb/β-PbO₂ anode. A new insight into the electrochemical degradation mechanism, *Appl. Catal. B Environ.* 261 (2020), 118226, <https://doi.org/10.1016/j.apcatb.2019.118226>.
 - [25] K. Barbari, R. Delimi, Z. Benredjem, S. Saaidia, A. Djemel, T. Chouchane, Nihal Oturan, M.A. Oturan, Photocatalytically-assisted electrooxidation of herbicide fenuron using a new bifunctional electrode PbO₂/SnO₂-Sb₂O₃/Ti/Ti/TiO₂, *Chemosphere* 203 (2018) 1–10, <https://doi.org/10.1016/j.chemosphere.2018.03.126>.
 - [26] Y. Jia, Y. Wen, X. Han, J. Qi, Z. Liu, S. Zhang, G. Li, Electrocatalytic degradation of rice straw lignin in alkaline solution through oxidation on a Ti/SnO₂-Sb₂O₃/α-PbO₂/β-PbO₂ anode and reduction on an iron or tin doped titanium cathode, *Catal. Sci. Technol.* 8 (2018) 4665–4677, <https://doi.org/10.1039/C8CY00307F>.
 - [27] L. Gan, Y. Wu, H. Song, C. Lu, S. Zhang, A. Li, Self-doped TiO₂ nanotube arrays for electrochemical mineralization of phenols, *Chemosphere* 226 (2019) 329–339, <https://doi.org/10.1016/j.chemosphere.2019.03.135>.
 - [28] Y. Yang, M.R. Hoffmann, Synthesis and stabilization of blue-black TiO₂ nanotube arrays for electrochemical oxidant generation and wastewater treatment, *Environ. Sci. Technol.* 50 (2016) 11888–11894, <https://doi.org/10.1021/acs.est.6b03540>.
 - [29] C. Kim, S. Kim, J. Choi, J. Lee, J.S. Kang, Y.-E. Sung, J. Lee, W. Choi, J. Yoon, Blue TiO₂ nanotube array as an oxidant generating novel anode material fabricated by simple cathodic polarization, *Electrochim. Acta* 141 (2014) 113–119, <https://doi.org/10.1016/j.electacta.2014.07.062>.
 - [30] D. Pang, Y. Liu, H. Song, D. Chen, W. Zhu, R. Liu, H. Yang, A. Li, S. Zhang, Trace Ti³⁺ and N-codoped TiO₂ nanotube array anode for significantly enhanced electrocatalytic degradation of tetracycline and metronidazole, *Chem. Eng. J.* 405 (2021), 126982, <https://doi.org/10.1016/j.cej.2020.126982>.
 - [31] L. Xu, J. Niu, H. Xie, X. Ma, Y. Zhu, J. Crittenden, Effective degradation of aqueous carbamazepine on a novel blue-colored TiO₂ nanotube arrays membrane filter anode, *J. Hazard. Mater.* 402 (2021) 12353, <https://doi.org/10.1016/j.jhazmat.2020.123530>.
 - [32] X. Qian, L. Xu, Y. Zhu, H. Yu, J. Niu, Removal of aqueous triclosan using TiO₂ nanotube arrays reactive membrane by sequential adsorption and electrochemical degradation, *Chem. Eng. J.* 420 (2021), 127615, <https://doi.org/10.1016/j.cej.2020.127615>.
 - [33] M.A. Ghanem, A.M. Al-Mayouf, M.N. Shaddad, F. Marken, Selective formation of hydrogen peroxide by oxygen reduction on TiO₂ nanotubes in alkaline media, *Electrochim. Acta* 174 (2015) 557–562, <https://doi.org/10.1016/j.electacta.2015.06.017>.
 - [34] J. Milikić, S. Marić, N. Cvjetičanin, Z. Dohčević-Mitrović, B. Šljukić, Facile preparation and high activity of TiO₂ nanotube arrays toward oxygen reduction in alkaline media, *J. Electrochem. Soc.* 165 (2018) J3253–J3258, <https://doi.org/10.1149/2.0331815jes>.
 - [35] H. Song, L. Yan, J. Ma, J. Jiang, G. Cai, W. Zhang, Z. Zhang, J. Zhang, T. Yang, Nonradical oxidation from electrochemical activation of peroxydisulfate at Ti/Pt anode: Efficiency, mechanism and influencing factors, *Water Res.* 116 (2017) 182–193, <https://doi.org/10.1016/j.watres.2017.03.035>.
 - [36] H. Song, L. Yan, J. Jiang, J. Ma, S. Pang, X. Zhai, W. Zhang, D. Li, Enhanced degradation of antibiotic sulfamethoxazole by electrochemical activation of PDS using carbon anodes, *Chem. Eng. J.* 344 (2018) 12–20, <https://doi.org/10.1016/j.cej.2018.03.050>.
 - [37] H. Song, L. Yan, J. Jiang, J. Ma, Z. Zhang, J. Zhang, P. Liu, T. Yang, Electrochemical activation of persulfates at BDD anode: radical or nonradical oxidation? *Water Res.* 128 (2018) 393–401, <https://doi.org/10.1016/j.watres.2017.10.018>.
 - [38] L. Bu, S. Zhu, S. Zhou, Degradation of atrazine by electrochemically activated persulfate using BDD anode: role of radicals and influencing factors, *Chemosphere* 195 (2018) 236–244, <https://doi.org/10.1016/j.chemosphere.2017.12.088>.
 - [39] W. Yang, G. Liu, Y. Chen, D. Miao, Q. Wei, H. Li, L. Ma, K. Zhou, L. Liu, Z. Yu, Persulfate enhanced electrochemical oxidation of highly toxic cyanide-containing organic wastewater using boron-doped diamond anode, *Chemosphere* 252 (2020), 126499, <https://doi.org/10.1016/j.chemosphere.2020.126499>.
 - [40] J. Cai, M. Zhou, Q. Zhang, Y. Tian, G. Song, The radical and non-radical oxidation mechanism of electrochemically activated persulfate process on different cathodes in divided and undivided cell, *J. Hazard. Mater.* 416 (2021), 125804, <https://doi.org/10.1016/j.jhazmat.2021.125804>.
 - [41] L. Bu, J. Ding, N. Zhu, M. Kong, Y. Wu, Z. Shi, S. Zhou, D.D. Dionysiou, Unraveling different mechanisms of persulfate activation by graphite felt anode and cathode to destruct contaminants of emerging concern, *Appl. Catal. B Environ.* 253 (2019) 140–148, <https://doi.org/10.1016/j.apcatb.2019.04.030>.
 - [42] A.J. dos Santos, E. Brillas, P.L. Cabot, I. Sirés, Simultaneous persulfate activation by electrogenerated H₂O₂ and anodic oxidation at a boron-doped diamond anode for the treatment of dye solutions, *Sci. Total Environ.* 747 (2020), 141541, <https://doi.org/10.1016/j.scitotenv.2020.141541>.
 - [43] Y. Rao, A. Li, Y. Zhang, F. Wang, T. Zhang, Y. Sheng, T. Jiao, Efficient degradation of metronidazole with dual-cathode of acetylene black-PTFE/CoFe₂O₄-PTFE coupling persulfate, *Sep. Purif. Technol.* 283 (2022), 120193, <https://doi.org/10.1016/j.seppur.2021.120193>.
 - [44] J. Sun, L. Liu, F. Yang, A visible-light-driven photocatalytic fuel cell/peroxymonosulfate (PFC/PMS) system using blue TiO₂ nanotube arrays (TNA) anode and Cu-Co-WO₃ cathode for enhanced oxidation of organic pollutant and ammonium nitrogen in real seawater, *Appl. Catal. B Environ.* 308 (2022), 121215, <https://doi.org/10.1016/j.apcatb.2022.121215>.
 - [45] W.-D. Zhu, C.-W. Wang, J.-B. Chen, Y. Li, J. Wang, Enhanced field emission from Ti³⁺ self-doped TiO₂ nanotube arrays synthesized by a facile cathodic reduction process, *Appl. Surf. Sci.* 301 (2014) 525–529, <https://doi.org/10.1016/j.apsusc.2014.02.116>.
 - [46] A. Naldoni, M. Alietta, S. Santangelo, M. Marelli, F. Fabbri, S. Cappelli, C. L. Bianchi, R. Psaro, V.D. Santo, Effect of nature and location of defects on bandgap narrowing in black TiO₂ nanoparticles, *J. Am. Chem. Soc.* 134 (2012) 7600, <https://doi.org/10.1021/ja3012676>.
 - [47] L. Burgio, R.J.H. Clark, S. Firth, Raman spectroscopy as a means for the identification of plattnerite (PbO₂), of lead pigments and of their degradation products, *Analyst* 126 (2001) 222–227, <https://doi.org/10.1039/B008302J>.
 - [48] M. Hayyan, M.A. Hashim, I.M. AlNashef, Superoxide ion: generation and chemical implications, *Chem. Rev.* 116 (2016) 3029–3085, <https://doi.org/10.1021/acs.chemrev.5b00407>.
 - [49] K. Wan, Z. Yu, X. Li, M. Liu, G. Yang, J. Piao, Z. Liang, pH effect on electrochemistry of nitrogen-doped carbon catalyst for oxygen reduction reaction, *ACS Catal.* 5 (2015) 4325–4332, <https://doi.org/10.1021/ACSCATAL.5B01089>.
 - [50] S.Y. Yang, H.W. Jeong, B.-j Kim, D.S. Han, W. Choid, H. Park, Electrocatalytic cogeneration of reactive oxygen species for synergistic water treatment, *Chem. Eng. J.* 358 (2019) 497–503, <https://doi.org/10.1016/j.cej.2018.09.192>.
 - [51] Y. Jing, B.P. Chaplin, Mechanistic study of the validity of using hydroxyl radical probes to characterize electrochemical advanced oxidation processes, *Environ. Sci. Technol.* 51 (2017) 2355–2365, <https://doi.org/10.1021/acs.est.6b05513>.
 - [52] Y. Pang, H. Xie, Y. Sun, M.-M. Titirici, G.-L. Chai, Electrochemical oxygen reduction for H₂O₂ production: catalysts, pH effects and mechanisms, *J. Mater. Chem. A* 8 (2020) 24996–25016, <https://doi.org/10.1039/D0TA09122G>.
 - [53] O.S. Furman, A.L. Teel, R.J. Watts, Mechanism of base activation of persulfate, *Environ. Sci. Technol.* 44 (2010) 6423–6428, <https://doi.org/10.1021/es1013714>.

- [54] Y. Zhu, S. Qiu, F. Deng, F. Ma, Y. Zheng, Degradation of sulfathiazole by electro-Fenton using a nitrogen-doped cathode and a BDD anode: Insight into the H_2O_2 generation and radical oxidation, *Sci. Total Environ.* 722 (2020), 137853, <https://doi.org/10.1016/j.scitotenv.2020.137853>.
- [55] Y. Xu, H. Lin, Y. Li, H. Zhang, The mechanism and efficiency of MnO_2 activated persulfate process coupled with electrolysis, *Sci. Total Environ.* 609 (2017) 644–654, <https://doi.org/10.1016/j.scitotenv.2017.07.151>.
- [56] A.J. dos Santos, P.L. Cabot, E. Brillas, I. Sirés, A comprehensive study on the electrochemical advanced oxidation of antihypertensive captopril in different cells and aqueous matrices, *Appl. Catal. B Environ.* 277 (2020), 119240, <https://doi.org/10.1016/j.apcatb.2020.119240>.
- [57] Z. Liu, C. Zhao, P. Wang, H. Zheng, Y. Sun, D.D. Dionysiou, Removal of carbamazepine in water by electro-activated carbon fiber-peroxydisulfate: Comparison, optimization, recycle, and mechanism study, *Chem. Eng. J.* 343 (2018) 28–36, <https://doi.org/10.1016/j.cej.2018.02.114>.
- [58] Y. Yu, W. Xu, J. Fang, D. Chen, T. Pan, W. Feng, Y. Liang, Z. Fang, Soft-template assisted construction of superstructure $TiO_2/SiO_2/g-C_3N_4$ hybrid as efficient visible-light photocatalysts to degrade berberine in seawater via an adsorption-photocatalysis synergy and mechanism insight, *Appl. Catal. B Environ.* 268 (2020), 118751, <https://doi.org/10.1016/j.apcatb.2020.118751>.
- [59] P. Ding, H. Ji, P. Li, Q. Liu, Y. Wu, M. Guo, Z. Zhou, S. Gao, W. Xu, W. Liu, Q. Wang, S. Chen, Visible-light degradation of antibiotics catalyzed by titania/zirconia/graphitic carbon nitride ternary nanocomposites: a combined experimental and theoretical study, *Appl. Catal. B Environ.* 300 (2022), 120633, <https://doi.org/10.1016/j.apcatb.2021.120633>.
- [60] Y. Zhang, L. Liu, B. Van der Bruggen, M.K.H. Leung, F. Yang, A free-standing 3D nano-composite photo-electrode-Ag/ZnO nanorods arrays on Ni foam effectively degrade berberine, *Chem. Eng. J.* 373 (2019) 179–191, <https://doi.org/10.1016/j.cej.2019.05.026>.
- [61] C.-F. Liu, C.P. Huang, C.-C. Hu, C. Huang, A dual TiO_2/Ti -stainless steel anode for the degradation of orange G in a coupling photoelectrochemical and photo-electro-Fenton system, *Sci. Total Environ.* 659 (2019) 221–229, <https://doi.org/10.1016/j.scitotenv.2018.12.224>.